The Functionalization of Magnetic Fe_3O_4@TiO_2 by Molecular Motif for the Detection of Mercury (II)

by

Jacquelyn G. Egan

A thesis submitted to the

School of Graduate and Postdoctoral Studies in partial

fulfillment of the requirements for the degree of

Master of Science in Material Science

The Faculty of Science

Ontario Tech University

Oshawa, Ontario, Canada

July, 2019

Abstract

2,6-bis(2-thienyl)pyridine (L) molecular receptor showed strong potential for Hg^{2+} detection. The chelation through S,N,S was confirmed as a main binding mode of the ligand with Hg^{2+} ion based on the results of ^{1}H NMR. L showed a strong characteristic fluorescence signal at 413 nm in the absence of Hg^{2+}; however, this signal was quenched when Hg^{2+} was introduced and a new fluorescence signal at 563 nm appeared. L was anchored into the surface of the coated magnetite microspheres (L-Fe_3O_4@TiO_2) through a siloxane template layer and was fully characterized using thermogravimetric analysis (TGA) and X-ray photoelectron spectroscopy (XPS). Detailed emission studies showed the ability of the L and L-Fe_3O_4@TiO_2 not only effectively detect Hg^{2+} but differentiate it from competing Zn^{2+}, Cd^{2+},Cu^{2+},Cr^{3+},Co^{2+},Ru^{3+}, Fe^{2+} ions in solution with minimum interference. Magnetic micropsheres decorated by L showed promising performance as single –excitation -single emission sensor for Hg^{2+} ions and effective mercury uptake.

Keywords: mercury; magnetite; fluorscence; surface sensor; thiophene

Author's Declaration

I hereby declare that this thesis consists of original work of which I have authored. This is a true copy of the thesis, including any required final revisions, as accepted by my examiners.

I authorize the University of Ontario Institute of Technology to lend this thesis to other institutions or individuals for the purpose of scholarly research. I further authorize University of Ontario Institute of Technology to reproduce this thesis by photocopying or by other means, in total or in part, at the request of other institutions or individuals for the purpose of scholarly research. I understand that my thesis will be made electronically available to the public.

Jacquelyn G. Egan

Statement of Contributions

Acknowledgements

Thank you Dr. Fedor Naumkin for performing Density Functional Theory (DFT) calculations on the metal complex. I would like to also thank Dr. Richard Bartholomew, Dr. Kevin Coulter and Prof. E Bradley Easton for allowing me to use various instruments in their labs for the synthesis and characterization of my materials. I would also like to thank the lab technician, Mike Allison for teaching me how to use the fluorimeter.

I would like to thank my fellow lab members, Nadia Laschuk and Holly Fruehwald, my two biggest assets and supporters in the lab. I am going to miss working with you deeply and wish you both the best on your PhD. Also to Holly Fruehwald, thank you for your electrochemical analysis of the materials. I would like to thank the rest of Zenkina lab, in particular, Sarah D. King and Alexandra Deckert for synthesizing the 2,6-di(thiophen-2-yl)-4,4'-bipyridine compound and for doing much of the initial solution sensing work with the ligand. As well as Andrew Hynes for measuring the cold vapour atomic absorption spectroscopy.

Finally, I would like to thank my supervisor Dr. Olena Zenkina for all the support and guidance over the course of my degree.

Table of Contents

List of Figures

1 Introduction

2 Experimental

3 Results and Disccusion

List of Abbreviations and Symbols

NMR: Nuclear Magnetic Resonance Spectroscopy

COSY: Correlation Spectroscopy NMR

HMBC: Heteronuclear Multiple Bond Correlation NMR

HSQC: Heteronuclear Single Quantum Coherence NMR

DEPT: Distortionless Enhancement by Polarization Transfer NMR

UV-vis: Ultra Violet – visible spectroscopy

TGA: Thermogravimetric analysis

DTG: Differential thermal analysis

BET: Brunauer-Emmett-Teller

EDX: Energy-dispersive X-ray spectroscopy

XPS: X-ray photoelectron spectroscopy

XRD: X-ray diffraction

SEM: Scanning electron microscopy

MLCT: Metal-to-Ligand Charge Transfer

PET: Photoinduced Electron Transfer

ICT: Intramolecular Charge Transfer

L: 2,6-bis(2-thienyl)pyridine

QL: 1-methyl-2',6'-di(thiophen-2-yl)-[4,4'-bipyridin]-1-ium

$Hg(ClO_4)_2$: Mercury (II) perchlorate hydrate

$Ru(bipy)_3$: Tris(2,2′-bipyridyl)dichlororuthenium(II) hexahydrate

Fe_3O_4: Magnetite

TiO_2: Titanium Dioxide

NP: Nanoparticles

ACN: Acetonitrile

List of Appendices

1 Introduction

1.1 Toxicity and Detection of Mercury

Mercury is a heavy metal and is known to be toxic due to its ability to act as a neurotoxin. Mercury can exist in three different forms, metallic mercury (Hg^0), inorganic mercury ($Hg^{1+/2+}$) and organic mercury (ex. methylmercury). Metallic mercury, which exists as a silver liquid, can be absorbed through the skin, and inhaled vapors can lead to severe lung damage and neurological disturbances. Inorganic mercury is mercury that has bonded with non-carbon compounds such as oxygen or chlorine, chronic exposure can lead to kidney abnormalities and memory problems. Organic mercury is bonded with carbon compounds and some forms have been known to bioaccumulate in many aquatic animals.[1] In 1963-1970, approximately 10 metric tons of mercury from an industrial plant in Dryden, Canada were released into the Wabigoon River, this leads to serious health issues to the indigenous people living in the area. Since then levels of mercury in the water have decreased and leveled off;[2] however, the removal of Hg^{2+} in these areas is still vital.

Current methods for monitoring Hg^{2+} in aqueous samples include atomic absorption spectroscopy (AAS)[3], inductively coupled plasma-mass spectrometry (ICP-MS)[4], electrochemical analysis[5] and fluorimetry[6]. Many of these methods such as AAS and ICP-MS have excellent sensitivity and selectivity but they are limited in their use as they require bulky and expensive equipment that is not typically portable. The users for many of these instruments also require advanced training. Alternatively, electrochemical analysis and fluorimetry are more portable, do not require advanced training, and the cost of instrumentation is decreased; however, they suffer lower sensitivity and selectivity. Thus,

the development of easy to use materials for the detection of Hg^{2+} in samples are of significant interest.

Fluorimetry is a highly sensitive optical technique compared to UV-vis and the equipment is simple to use. Fluorescence sensors can be categorized as either "turn on" or "turn off" sensors, depending on how the fluorescence peak changes with the increase in analyte concentration. If the fluorescence peak signal decreases with the increase of analyte it is defined as a "turn off" fluorescence sensor. If the opposite is true and the fluorescence signal increases with the increase of analyte then it is a "turn on" fluorescence sensor. This work will focus on the formation of a fluorescent coordination complex between Hg^{2+} and a heterocyclic ligand that shows potential as a turn off/on sensor.

1.2 Solution Chemistry of Hg^{2+}

The coordination chemistry of mercury is an interesting field because mercury is very reactive and its complexes can have interesting electrochemical, fluorescence, and absorbance properties. Coordination compounds of mercury have long been explored by chemists as they have promising catalyst applications.[7] According to the Pearson Hard Acid Soft Base (HSAB) theory, larger and less electropositive metals in low oxidation states such as $Hg^{1+/2+}$ are considered soft Lewis acids, these are able to form stable complexes with less electronegative donor atoms, soft Lewis bases, such as carbon, sulfur, arsenic, and iodine.[8]

Of all the oxidation states of mercury, Hg^{2+} has the strongest tendency to form complexes with a wide variety of organic ligands. The typical geometries of Hg^{2+} complexes are two coordinate (linear) and four coordinate (tetrahedral) geometries. The large ionic radius of Hg^{2+} favors the formation of higher coordination number complexes

with a suitable donor through an associative process, making the ligand exchange mechanism possible. The most stable complexes are formed using ligands that include carbon, nitrogen, phosphorus and sulfur atoms. The different ligands are expected to have different strength of the interactions between Hg^{2+} ions and "soft" sulfur-donors have a stronger interaction with mercury than "harder" nitrogen and oxygen donors. However, often molecular receptors that contain both nitrogen/oxygen and sulfur centers will demonstrate effective cooperative binding with Hg^{2+} ions. For example, dibenzamide derivatives with a thioether linker[9] showed high chelation ability by both nitrogen and sulfur atoms with high sensitivity to fluorimetric mercury detection and the only major interference with Fe^{3+} ions. Many different coordination modes are plausible for compounds containing both sulfur and nitrogen binding centers. While binding via Hg^{2+}-S interactions often reported as the kinetically favourable product, binding to nitrogen and/or carbon centers believed to be more thermodynamically stable.

1.3 Heterocyclic Ligands for Optical Sensors of Metals

Heterocyclic ligands are ring structures containing one or more atoms that are different from the member of its ring. The use of heterocyclic ligands for optical and electrochemical sensors with transition metals has been intensively explored.[10] Thiophene/pyridine based heterocyclic ligands have been shown to act as a turn off / turn on sensors in the presence of Hg^{2+}.[11] Thiophenes contain a sulfur group which according to the HSAB theory is a soft base and should be strongly attracted to Hg^{2+} which is a soft acid, improving the selectivity of the ligand. The Hg^{2+} ion can impact the fluorescence of the thiophene/pyridine head group through an intramolecular charge transfer (ICT) mechanism.[12] During excitation of the system, the thiophene/pyridine undergoes donor-

acceptor intramolecular charge transfer which strongly depends on the environment of the thiophene/pyridine. The Hg^{2+} affects the ICT efficiency that changes the energy between the ground and excited state and results in the variation of the fluorescence. However, some reported molecular systems containing both sulfur and nitrogen/oxygen centers have preferential binding not necessary involving the sulfur atoms. For example, receptors containing sulfur, oxygen and nitrogen binding center have a tendency to coordinate mercury ion mainly via nitrogen and oxygen atoms while the sulfur is left intact.[13]
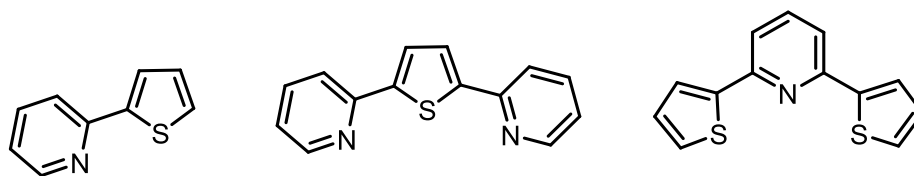
Figure 1.1 Chemical structure of different thiophene/pyridine-based head groups

1.4 Functionalization of Molecular Receptors on the Surface

Nanomaterials and micromaterials for the detection of different analytes have gained a great deal of attention due to their high surface area to volume ratio as well as their size-dependent properties, such as color and conductivity. Gold nanoparticles and quantum dots are often utilized for the detection of mercury.[14] However, bare plasmonic metal-based nanomaterials are very expensive and may not have the ideal selectivity. Grafting organic molecular receptors onto the surface allows for the fine-tuning of the properties of the nanosurfaces.

Hydrophilic surfaces (as silicon oxide, glass and metal oxide surfaces) will allow for the effective self-assembly of ligands onto the surface through a number of different linkers such as silanes/siloxanes,[15] phosphonic acids[16] and dopamine.[17] Each linker has its own

unique advantages and disadvantages and normally chosen based on the application of the material and silanes are often chosen since they form very strong bonds to the surface. Linkers such as phosphonic acid and carboxylic acids are easily able to be deposited on the surface; however, the bond they form to the surface are only moderately stable and could be broken especially in strongly acidic conditions. Alternatively, silanes/siloxanes require "moisture-free "deposition conditions (traces of water initiate the undesirable process of self-condensation); however, they form very strong bonds to the hydrophilic surface, thus improving the stability of the monolayer.

The head group of the ligand is also critical because it is normally designed to give the nanomaterials desired properties. The use of ligands with high affinity for Hg^{2+} attached to noble metal nanostructures proved to be a highly sensitive alternative when compared to bare plasmonic metal structures. For example, gold nanorods functionalized with 1-[2-(octylamino)ethyl]-3,5-diphenylpyrazole, were able to coordinate heavy metal ions. In particular, the exposure of the functionalized gold nanorods to increasing amounts of Hg^{2+} ions has resulted in a gradual sensitive color change from pink color to purple color.[18] Alternatively, alkanethiol-based capping agents are capable of preventing leaching of plasmonic metal ions (silver/gold) from the nanosurface to solution by formation of soluble metal salts, metal complexes and metal clusters; as well as effectively and selectively interacting with Hg^{2+} ions. The presence of Hg^{2+} ions in a solution of silver nanoparticles caused the detachment of the adsorbed alkanethiols from the surface of some nanoparticles resulting in the aggregation of nanoparticles that could be easily detected by a significant color changes.[19] As mentioned before, these nanomaterials can be expensive and finding an affordable alternative is a future direction for these hybrid sensors. Alternatively,

fluorescent dopamine–naphthalimide–dipicolylamine, capable of acting as a sensing receptor for Zn^{2+}, was immobilized onto the surface of magnetite nanoparticles to prepare a hybrid sensor that was reusable and sensitive.[17]

1.5 Magnetite-based Nanomaterials for Sensing and Metal Uptake.

Magnetite (Fe_3O_4) is a common iron ore that can be found in the earth's crust. Of all the iron oxides, it is known to be the most magnetic material. Its abundance makes it a relatively inexpensive material to work with and its magnetic properties make it useful in a number of different applications. Magnetite nanoparticles (Fe_3O_4 NP) are known to have ferrimagnetic properties and a number of uses in different applications such as magnetic resonance imaging (MRI), water treatment, and catalysis.[20] Recently, groups have been able to detect metals such as Cu^{2+} and Zn^{2+} by functionalizing the surface of the Fe_3O_4 NP with ligands that show high selectivity and sensitivity to these metals as fluorescence "turn on" sensors.[15a, 17] These magnetic materials not only allowed for the monitoring of metals but also the recycling of them as well.

The coating of magnetite nanoparticles offers the advantage of keeping a magnetic core while changing the properties and surface chemistry of the nanoparticles. Researchers have coated magnetite with semiconductor materials such as SiO_2 and TiO_2 in order to develop recyclable photocatalysts as well as heavy metal uptake systems.[21] The coating can also offer protection for the magnetic core from other strains. As mentioned before, thiophene/pyridine based head groups have been shown to be good sensors for mercury (II); however, they have also shown a high affinity for iron (III). To prevent leaching of iron ions off the surface of the Fe_3O_4 a layer of TiO_2 was coated on the magnetite core. The TiO_2 still granting the hydrophilic surface for the creation of the siloxane templating layer

6

that is necessary to introduce the molecule of interest into the material but minimizes the influence of the iron (III) in Fe_3O_4.

In this work, 2,6-bis(2-thienyl)pyridine (L) was shown to complex to Hg^{2+}, the complex between Hg^{2+} and L was synthesized with a 25% yield. It was characterized using nuclear magnetic resonance (NMR), such as ^{1}H-NMR and ^{13}C{H}-NMR, and ultraviolet-visible (UV-vis) spectroscopy. The proposed structure of Hg^{2+}-L is an SNS coordination mode with two thiophene rings and middle pyridine unit forming a symmetric chelate with the Hg^{2+} center was supported by the ^{1}H-NMR and ^{13}C{H}-NMR. L has a strong characteristic fluorescence signal at 413 nm upon excitation at 380 nm in the absence of Hg^{2+}; however, this signal was quenched when Hg^{2+} was introduced and a new fluorescence signal at 563 nm appeared. Showing its potential as a turn on/off fluorescence sensor. While Cu^{2+}, Co^{2+}, Cd^{2+} and Zn^{2+} did affect the 413 nm emission peak the completing ions could still be distinguished from Hg^{2+} since the "turn-on" emission peak at 563 nm only occurred due the formation of the Hg^{2+}-L complex. No significant interference was observed with Ru^{3+} since their complexes are less kinetically favorable than Hg^{2+}. No significant interference was observed with the addition of Cr^{3+} which could be explained by the electron count. Similarly, Fe^{2+} could easily be differentiated from Hg^{2+} since it does not significantly quench 413 nm peak and does not cause a strong emission peak at 563 nm to appear. The major interference occurred with Fe^{3+} since it caused quenching of the 413 nm peak as well as a strong emission peak at 563 nm.

The Fe_3O_4@TiO_2 were synthesized using a literature procedure and characterized using X-ray diffraction (XRD) and scanning electron microscopy (SEM). Next, L was anchored into the surface of the coated magnetite microspheres (L-Fe_3O_4@TiO_2) through a siloxane

template layer and was fully characterized using thermogravimetric analysis (TGA) and X-ray photoelectron spectroscopy (XPS). The sensitivity of L-Fe$_3$O$_4$@TiO$_2$ for Hg^{2+} was determined by measuring the fluorescent signal at 413 nm and the XPS of the material in the presence of Hg^{2+}. Changes in the fluorescence spectra for L-Fe$_3$O$_4$@TiO$_2$ were due to quarterization of L onto the surface. Finally, the selectivity of the material was determined by measuring the characteristic fluorescence signal at 413 nm of L-Fe$_3$O$_4$@TiO$_2$ NP in the presence of several metals with and without Hg^{2+}. Slight changes in sensitivity were observed and could be explained by the availability of L on the surface; however, it was possible to sense Hg^{2+} with little interference from competing ions.
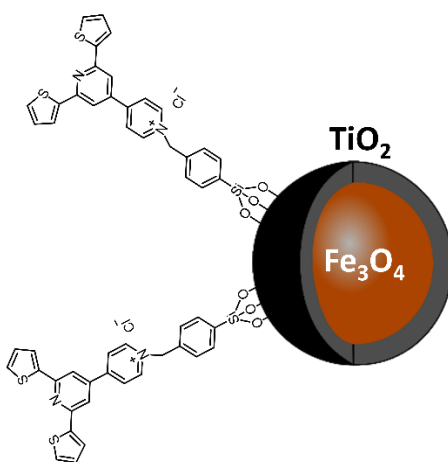
*Figure 1.2 Chemical structure of 2,6-di(thiophen-2-yl)-4,4'-bipyridine (**L**) bonded to Fe$_3$O$_4$@TiO$_2$ through a siloxane linker*

2 Experimental

2.1 Materials and Instrumentation

Chemicals were purchased from Sigma-Aldrich, VWR and Alfa Aesar. Deuterated solvents were purchased from Cambridge Isotope Laboratories. All reagents were used

without further purification with the exception of dry solvents which were bubbled with N_2 for 15 min, and left under an inert atmosphere with oven-dried molecular sieves at least 24 h. For all air-sensitive reactions (like deposition of the silane template and metal complex), glassware was dried overnight at 130^oC.

All Nuclear Magnetic Resonance (NMR) measurements were recorded on a Bruker 400 Advance III MHz spectrometer. Fluorescence spectra were measured on a Cary Eclipse in a 10 mm x 10 mm quartz cuvette. UV-visible spectra were measured on an Agilent Cary 60 UV-Vis Spectrophotometer. X-ray diffraction (XRD) measurements were performed on the Rigaku Ultima IV X-ray diffractometer that employs using Cu Kα radiation (λ = 0.15418nm) Diffraction patterns were obtained over a 2θ range of 20–80° using a step size of 0.02°. Brunauer-Emmett-Teller (BET) was measured using a Quantachrome NOVAe 1200 pore size analyzer. Scanning Electron microscopy (SEM) images and energy dispersive x-ray analysis (EDX) were performed using a Hitachi FlexSEM 1000. Thermogravimetric analysis (TGA) using a TA Instruments Q600 SDT thermal analyzer. The samples were heated at 5^0C min^{-1} from room temperature to 1000^0C while flowing air (10 mL/min). X-ray photoelectron spectroscopy (XPS) measurements were performed on a Thermo Scientific K-Alpha spectrophotometer equipped with an Al Kα (1486.6 eV) X-ray source. The binding energies were referenced to the Au 4f7/2 peak at 84.0 eV.

2.2 Synthesis and Characterization of Hg^{2+}-L Complex

The Hg^{2+}-L complex was synthesized in an acetonitrile solution prepared by addition to the solution of L (24.2 mg, 0.076 mmol) with 1 equiv. of mercury(II) perchlorate hydrate (30 mg, 0.076 mmol). After 30 min, yellow precipitate was formed from the solution, was filtered out and washed with 50 mL of hexanes resulting in 10 mg, 25 % yield of complex Hg^{2+}-L. ^{1}H NMR (400 MHz, CD$_3$CN) δ 8.88 (d, ^{3}J$_{HH}$ = 6.1 Hz, 1H), 8.49 (d, ^{3}J$_{HH}$ = 6.2 Hz, 1H), 8.07 (s, 1H), 7.92 (d, ^{3}J$_{HH}$ = 3.6 Hz, 1H), 7.65 (d, ^{3}J$_{HH}$= 5.0 Hz, 1H), 7.3 Hz (m, 1H). ^{13}C-NMR (101 MHz, CD$_3$CN) δ: 155.65 (Cq), 152.7 (Cq), 145.5 (Cq), 142.15, 130.4 (Cq), 130.1, 128.7, 127.3, 125.8, 116.5. (Note: Quaternary carbons were not well resolved and were located and assigned with the help of ^{1}H-^{13}C-HMBC NMR.)
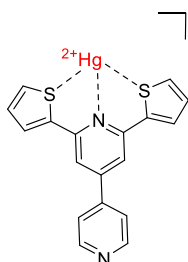
The Hg^{2+}-QL (QL= quaternized L) complex was synthesized in an acetonitrile solution prepared by addition to the solution of L (27 mg, 0.058 mmol) with 1 equiv. of mercury(II) perchlorate hydrate (23.4 mg, 0.058 mmol). After 30 min yellow precipitate was formed from the solution, was filtered out and washed with 50 mL of hexanes resulting in 7.6 mg, 17.8% yield of complex Hg^{2+}-QL. ^{1}H NMR (400 MHz, CD$_3$CN) δ 8.81 (d, ^{3}J$_{HH}$ = 7.24 Hz, 1H), 8.46 (d, ^{3}J$_{HH}$ = 7.24 Hz, 1H), 8.09 (s, 1H), 7.94 (d, ^{3}J$_{HH}$ = 4.84 Hz, 1H), 7.71 (d, ^{3}J$_{HH}$= 6.04 Hz, 1H), 7.28 (m, 1H), 4.39 (s, 3H). ^{13}C-NMR (101 MHz, CD$_3$CN) δ: 153.1(Cq), 152.6(Cq), 145.9, 144.7(Cq), 137.7(Cq), 130.2, 128.7, 127.7, 126.1, 116.1, 48.21
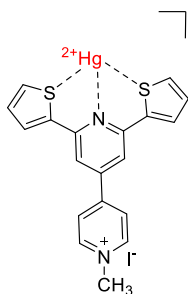
The UV-vis of the Hg^{2+}-L complex was done by making a stock solution of L was made by dissolving L in ACN giving a concentration of 0.04 mM. This was then transferred to a 10 mm x 10 mm quartz cuvette. The UV-vis spectra were measured from λ$_{em}$ = 200 – 800

nm at a medium scan rate. An aliquot of 1.0 µL of an Hg^{2+} solution with a concentration of 20.67 mM was added to the solution of L, then the UV-vis spectra were measured from $\lambda_{em} = 200 - 800$ nm at a medium scan rate.

2.3 Characterization of Sensing Ability in Solution

A stock solution of L was made by dissolving L in ACN obtaining a concentration of 0.04 mM. The solution was then transferred to a 10 mm x 10 mm quartz cuvette. The fluorescence emission was measured using $\lambda_{ex} = 380$ nm and $\lambda_{em} = 400 - 700$ nm at a medium scan rate. A solution of Hg^{2+} with a concentration of 20.67 mM was added dropwise to the solution in intervals of 1.0 µL using a syringe.

Seven metal solutions were prepared by dissolving the metal salt in ACN to make up a stock solution. A stock solution of L was made by dissolving L in ACN obtaining a concentration of 0.04 mM. The solution was then transferred to a 10 mm x 10 mm quartz cuvette. The fluorescence emission was measured using $\lambda_{ex} = 380$ nm and $\lambda_{em} = 400 - 700$ nm. An aliquot of the first metal solution was added to the cuvette then stirred for 2 minutes. Next, the fluorescence emission of M+L was measured. Lastly, Hg^{2+} was added to the cuvette before the UV-vis and fluorescence emission of $M + L + Hg^{2+}$ was obtained. These steps were repeated for all seven metal salts.

2.4 Quantum Yield of Hg^{2+}-L Complex

The quantum yield of Hg^{2+}-L was determined using the fluorescent standard sample $Ru(bipy)_3$ as its λ_{abs} and λ_{em} are similar to that of the Hg^{2+}-L complex test sample.[22] A stock solution of $Ru(bipy)_3$ was prepared by dissolving $Ru(bipy)_3$ in DI water to give a concentration of 0.2 mM. A stock solution of Hg^{2+}-L was prepared by dissolving L and

$Hg(ClO_4)^{2+}$ in ACN. The Hg^{2+}-L product was filtered out and dissolved in ACN obtaining a final concentration of 0.67 mM solution.

The UV-Vis absorbance of the solvent background was measured, followed by eleven dilutions of the standard Ru(bipy)$_3$ stock solution. The fluorescence emission was also measured using λ_{ex} = 452 nm and λ_{em} = 460 – 700 nm. This was repeated for the Hg^{2+}-L test sample, fluorescence emission was measured using λ_{ex} = 380 nm and λ_{em} = 400 – 700 nm. The integrated fluorescence intensity was plotted against the absorbance at the fluorometer excitation wavelength. This is at 452 nm for Ru(bipy)$_3$ and 380 nm for Hg^{2+}-L. A linear regression line was fitted to the resulting graph, of which the gradient is required for the quantum yield calculation.

Equation 1[23] is required to calculate the fluorescence quantum yield:

$$\varphi_x = \varphi_{STD} \left(\frac{m_x}{m_{STD}} \right) \left(\frac{\eta_x^2}{\eta_{STD}^2} \right) \tag{1}$$

Where 'x' denotes the complex (test sample) and 'STD' denotes Ru(bipy)$_3$ (standard sample). φ represents the quantum yield, m represents the gradient of the plot of integrated fluorescence intensity vs absorbance, and η represents the refractive index of the solvent used.

2.5 Synthesis of Microspheres

The synthesis of Fe_3O_4 was carried out according to a previously reported method with modification,[21c, 24] 2.5g of $FeCl_3 \cdot 6H_2O$ was allowed to stir in 75 mL of ethylene glycol until it dissolved. Then 7.2g of NaAc and 2g of PEG 4000 were added to the above solution and stirred until all the reactants dissolved. The mixture was then transferred into a Teflon-lined stainless-steel autoclave. The autoclave was heated to and maintained at 160°C for 8

hours and then naturally cooled to room temperature. The product mixture was centrifuged, and the liquid was discarded while the solids were washed with ethanol and water. The magnetite product was dried under vacuum at 90°C for 10 hours.

The synthesis of $Fe_3O_4@TiO_2$ was based on a previous method,[25] 100 mg of Fe_3O_4 microspheres were dispersed in 100 mL of an ethanol/ACN (3/1, v/v), followed by the addition of 1 mL concentrated ammonia solution (28%) under sonication for 20 minutes. Afterward, 1.6 mL of TBOT in 30 mL of ethanol/ACN (3/1, v/v) was added dropwise under continuous sonication. The mixture was then allowed to stir under sonication for 2 hours then transferred into a Teflon-lined stainless-steel autoclave. The autoclave was heated to and maintained at 160°C for 24 hours and then naturally cooled to room temperature. The product mixture was centrifuged, the liquid was discarded while the solids were washed with ethanol and water. The product was then dried under vacuum at 100°C overnight. The powder was sonicated in solutions of ethanol and water multiple times then separated with a magnet to remove any unreacted TiO_2.

2.6 Functionalization of $Fe_3O_4@TiO_2$ with L

The solid substrates were functionalized in the glove box according to an adapted literature procedure.[15b, 26] Under N_2 atmosphere, substrates were submerged into a solution of trichloro(4- (chloromethyl)phenyl)silane with dry hexane (1:200 v/v) for 20 min. Materials were washed 3x with dry hexane then dry ACN, and sonicated 1x for 5 min per solvent.
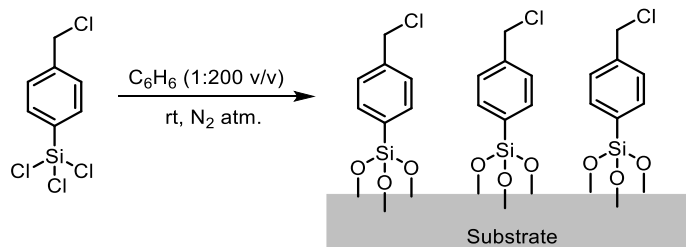
Figure 2.1 Deposition of siloxane onto the hydrophilic surface

L solutions (0.2 mM) were premade in dry ACN. Under inert atmosphere, the powder was submerged into a solution of the ligand and sealed in a pressure tube. Materials were heated for 96 h at 95°C without light. After cooling down, materials were washed 3x with dry hexane then dry ACN, and sonicated 1x for 5 min per solvent.
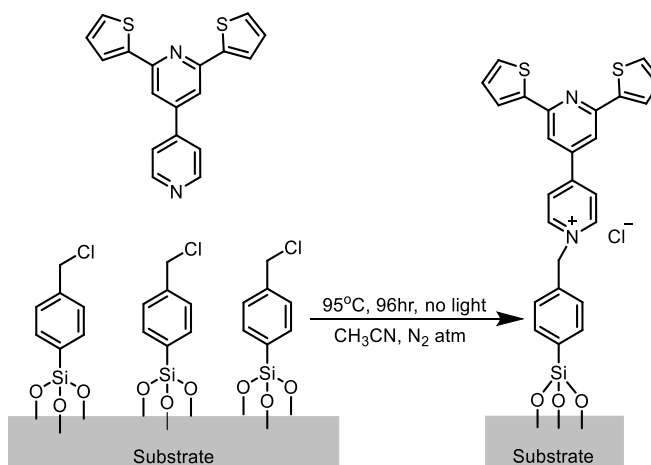
Figure 2.2 Quaternization of L onto siloxane linker

2.7 Characterization of sensing ability of the L-Fe₃O₄@TiO₂

The fluorescence of L-Fe$_3$O$_4$@TiO$_2$ was measured by adding 1.0 mg of sample into 3.0 mL of dried ACN and sonicating it for 15 minutes. The solution was then transferred to a 10 mm x 10 mm quartz cuvette. The fluorescence emission was measured using $\lambda_{ex} = 330$ nm and $\lambda_{em} = 340 - 600$ nm at a slow scan rate. A solution of Hg^{2+} with a concentration of

20.67 mM was added drop wise to the solution in intervals of 1.0 µL using a syringe, the fluorescence spectra of the L-Fe_3O_4@TiO_2 with Hg^{2+} were measured three times each to obtain the average peak height. Between each run and addition, the solution was mixed for 30 seconds before the fluorescence emission was measured.

Seven metal solutions were prepared by dissolving the metal salt in ACN. For the fluorescence spectra, 1.0 mg of L-Fe_3O_4@TiO_2 was added into 3.0 mL of dried ACN and sonicated for 15 minutes then transferred to a 10 mm x 10 mm quartz cuvette. The fluorescence emission was measured using λ_{ex} = 330 nm and λ_{em} = 340 – 600 nm. An aliquot of the first metal solution was added to the cuvette, sonicated for 2 minutes. Then the fluorescence emission of M+L was measured. Lastly, Hg^{2+} was added to the cuvette, sonicated for 2 minutes before the UV-vis and fluorescence emission of M + L + Hg^{2+} was obtained. These steps were repeated for all seven metal salts.

3 Results and Discussion

3.1 Analysis of Hg^{2+}-L complex

The complex between Hg^{2+} and L was synthesized with a 25% yield. It was characterized using ^{1}H-NMR and ^{13}C{H}-NMR. The proposed structure of Hg^{2+}-L is an SNS coordination mode with two thiophene rings and middle pyridine unit forming a symmetric chelate with the mercury center (Figure 3.1). The ^{1}H-NMR (Appendix One) showed no evidence of hydrogen abstraction and the formation of an asymmetrical CNS-complex. Deshielding typically occurs due to increased proximity to an electron withdrawing group and leads a downfield shift of the proton peaks. There is a significant downfield shift for characteristic doublets corresponding to non-chelating pyridine ring (H_E and H_F) from 8.78 and 8.04 ppm in the free ligand to 8.90 and 8.49 ppm, respectively.

In addition, singlet resonance at 8.22 ppm of the protons of chelating pyridine ring (H_D) and doublet resonance at 8.07 ppm for the thiophene protons (H_C) become noticeably shifted up field. These observations are fully consistent with an SNS coordination mode. The peak positions in the ^{1}H-NMR were also confirmed by ^{1}H-^{1}H COSY NMR, which is shown in Appendix Three.

The structure was also characterized using ^{13}C{H}-NMR, shown in Appendix Two, it showed seven peaks of the possible ten carbon peaks in L (Figure 3.1). The seven peaks corresponded to the six tertiary carbons and one quaternary carbon. Due to the limited solubility of Hg^{2+}-L it was difficult to get a signal from the quaternary carbons using only ^{13}C{H}-NMR. Instead, 2D ^{1}H-^{13}C NMR technique was used to correlate protons to their corresponding carbons. The chemical shifts of all six tertiary carbons were confirmed by ^{1}H-^{13}C-HSQC NMR (Appendix Five) and DEPT135 NMR (Appendix Six), these techniques correlate protons with carbons that are directly bonded to one another (^{1}J correlation). The other three remaining quaternary carbons were resolved using ^{1}H-^{13}C-HMBC NMR (Appendix Four), this technique correlates protons with carbons that are separated by more than one bond(^{2}J-^{3}J correlation). Once resolved they are assigned according to their chemical shift and proximity to electron withdrawing groups. All methods support that a complex was formed between Hg^{2+} and L in the purposed 1:1 SNS coordination.
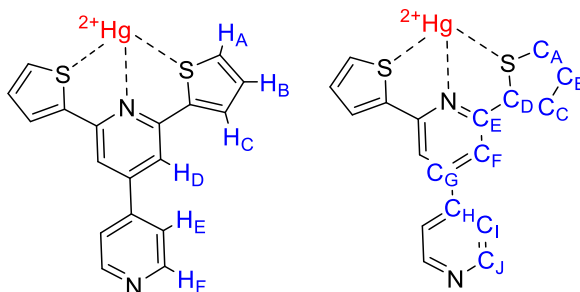
Figure 3.1 Structures of Hg^{2+}-L with protons and carbons highlighted

The complex between Hg^{2+}-L was also characterized using UV-vis spectroscopy, which is shown in Figure 3.2, it also shows a photograph of the Hg^{2+}-L complexes suspended in ACN. The UV-vis spectroscopy shown Hg^{2+}-L absorbing light around 230 nm to 330 nm, with the appearance of a distinct peak at 330 nm. The absorbance of high energy wavelengths also contributes to the yellow color of the complexes as shown in the photo in Figure 3.2. This supports the idea that a complex between L and Hg^{2+} has been formed.
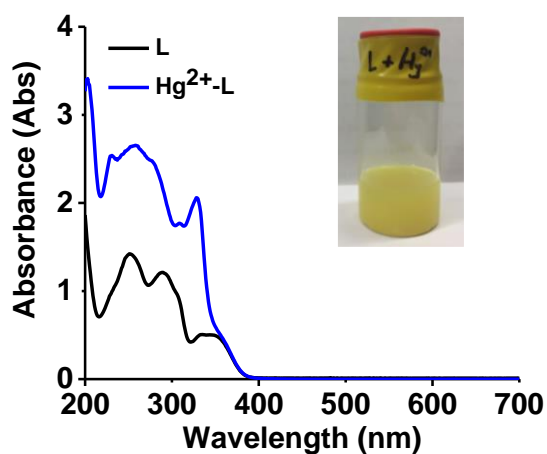
Figure 3.2 UV-vis spectra of 0.04 mM L and Hg^{2+}-L in ACN; photo of 0.04 mM Hg^{2+}-L in ACN

17

3.2 Sensing Hg²⁺ in Solution

The Hg^{2+} affects the ICT efficiency and changes the energy between the ground and excited state which results in the variation of the fluorescence. L showed a strong characteristic fluorescence signal at 413 nm in the absence of Hg^{2+}, this signal was quenched linearly when Hg^{2+} was introduced and a new fluorescence signal at 563 nm corresponding to Hg^{2+}-L increased linearly. This red shift from 413 nm to 563 nm in the fluorescence signal is shown in the spectra (Figure 3.3 A). The photo shows L and Hg^{2+}-L under an UV light (365 nm), free L in solution emitted in the blue region but when Hg^{2+} is added there is a red shift and the Hg^{2+}-L complex emitted in the yellow region. In the emission spectra, a single isosbestic point is observed at 500 nm. This supports the idea that there is a single transition from L to Hg^{2+}-L without any intermediates forming in between. The calibration curve was calculated (Figure 3.3 B and C) for both the peak at 413 nm and 563 nm, the calibration curve for the "turn off" sensor of the 413 nm peak had a good fit of $R^2 = 0.96$ in the region between 0 ppm and 8 ppm, beyond this point the fluorescent emission of L become quenched. The LOD determined from the first curve is 1.4 ppm of Hg^{2+}. The calibration curve for the turn peak at 563 nm had a similarly good correlation of $R^2 = 0.96$ in the region between 0 ppm and 8 ppm, beyond this point there is a still a linear trend; however, the slope changes. The LOD determined from this curve is again 1.4 ppm of Hg^{2+}. As a result, L can be considered as a rear single excitation – dual emission ratiometric mercury sensor in the solution.
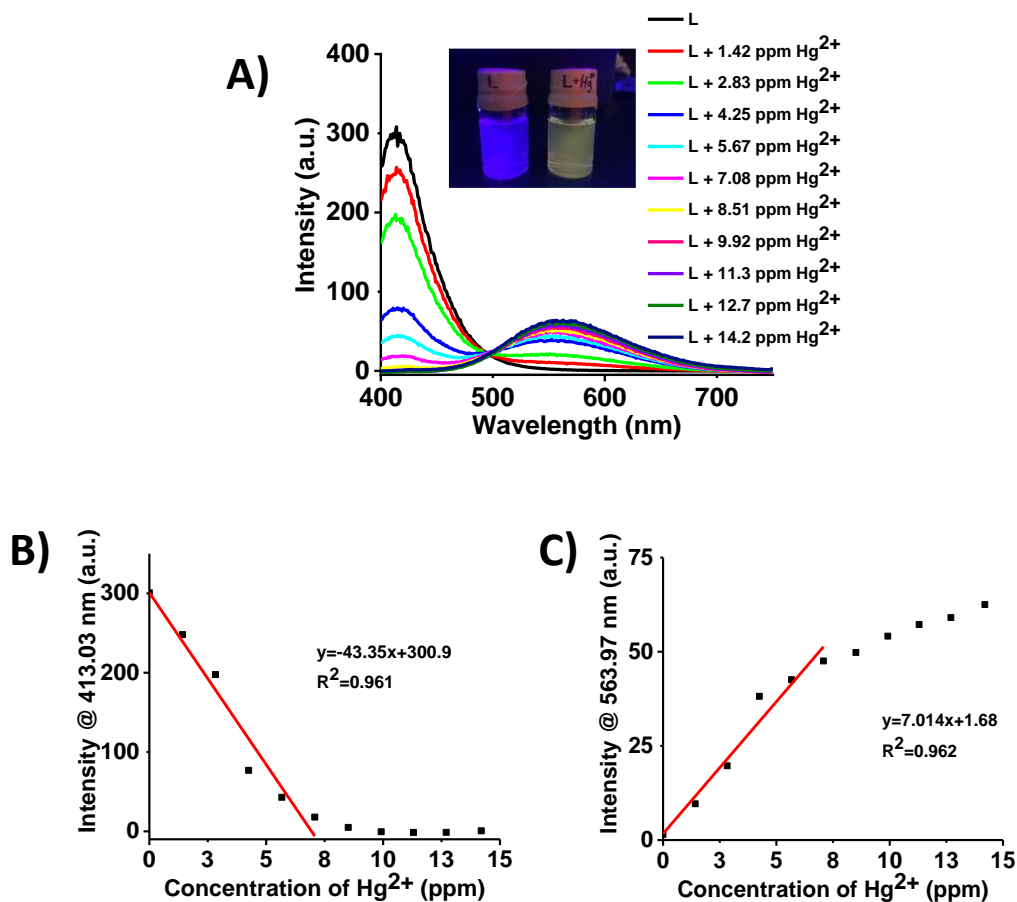
*Figure 3.3 **A)** Photo of L and Hg^{2+}-L in ACN under UV 365 nm light and emission spectra of L in ACN with increasing concentrations of Hg^{2+} **B)** Calibration curve of L using the peak intensity from the 413 nm emission peak **C)** Calibration curve of L using the peak intensity from the 563 nm emission peak*

The fluorescence quantum yield (QY) is defined as the ratio of the number of photons emitted to the number of photons absorbed. A Ru(bipy)$_2$ complex was used as the fluorescence standard in order to determine the QY of the Hg^{2+}-L complex since they had similar excitation and emission wavelengths; the calibration curves and standard error calculations are shown in Appendix Twelve and Thirteen. The quantum yield of the Hg^{2+}-L complex was found to be 57% which is very high QY, and these results are consistent

with QY values of the emission for the previously reported Hg^{2+} complexes with thiophenes.[27]

In order to evaluate the selectivity of L for Hg^{2+} a competitor ion was added to L, the emission spectrum was measured, and then Hg^{2+} was added. This was to see not only if the competitor ion would produce the same response as Hg^{2+} but also how it may impair Hg^{2+} from binding to L. The bar graphs shown in Figure 3.4 depict the selectivity for the fluorescence signal of L at 413 nm and 563 nm. For the two major d^{10} metals competitors, Cd^{2+} and Zn^{2+} do not cause the 413 nm emission peak to quench significantly but they do seem to bond to L preventing Hg^{2+} from bonding and fully quenching the 413 emission peak. However, L is still selective for Hg^{2+} over Cd^{2+} and Zn^{2+} since a strong emission peak at 563 nm which is due to the formation of the Hg^{2+}-L complex still occurs. Similarly, the addition of Cu^{2+} and Co^{2+} to L also caused quenching in the 413 nm signal the strong emission peak at 563 nm only occurred once Hg^{2+} was added. Fe^{2+} can easily be differentiated from Hg^{2+} since it does not significantly quench 413 nm peak and a strong emission peak at 563 nm is only seen with the addition of Hg^{2+}. This is not the case for Fe^{3+}, there is significant quenching of the 413 nm peak, as well as rapid growth of the emission peak at 563 nm, occurs when Fe^{3+} is added to L in the absence of Hg^{2+}. While Ru^{3+} is also known to have a very similar electron configuration to Fe^{3+} meaning it should form a similar complex it requires higher temperatures to form stable complexes with pyridines making it less kinetically favorable than Hg^{2+}.[16b, 28] No significant quenching is observed with the addition of Cr^{3+}. Typically, stable metal complexes have an electron count of 16 or 18 electrons, however; the complexes formed with Cr^{3+} is 15 electrons which make complexes fairly reactive. It was possible to distinguish Hg^{2+} from competing Zn^{2+},

Cd^{2+}, Cu^{2+}, Cr^{3+}, Co^{2+}, Ru^{3+}, Fe^{2+} ions in solution with minimum interference using both the "turn off" emission peak at 413 nm and the "turn-on" emission peak at 563 nm.
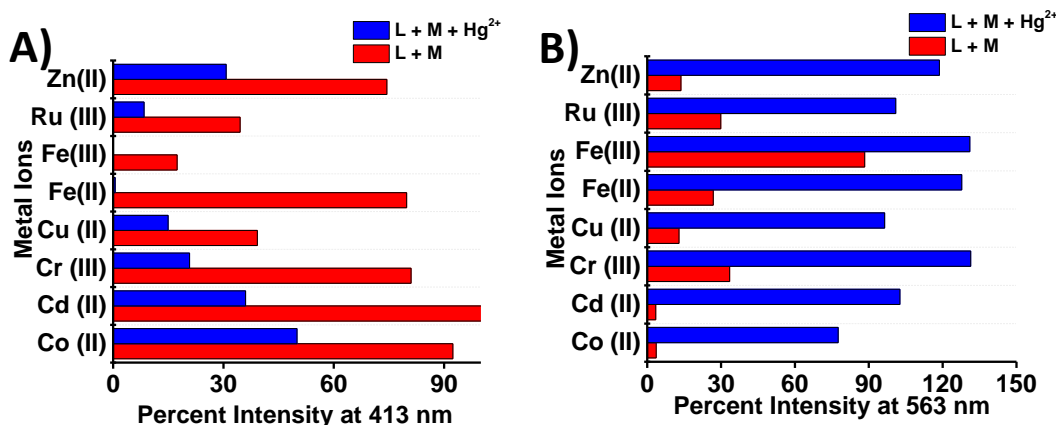

*Figure 3.4 The selectivity of L in the presence of several transition metals (Cr^{3+}, Zn^{2+}, Fe$^{3+/2+}$, Co^{2+}, Ru^{3+}, Cd^{2+}, Cu^{2+}) in ACN **A**) at the 413 nm emission peak **B**) at* the 563 nm emission peak

Once it was confirmed that L was capable as a fairly selective "turn on"/"turn off" fluorimetric sensor for Hg^{2+} the next step was to put it on the surface of Fe$_3$O$_4$. As seen in from the selectivity L is quenched significantly in the presence of Fe^{3+}; to reduce the risk of an iron leaching effect, the emission signal of L the Fe$_3$O$_4$ will be first coated with TiO$_2$.

3.3 Physical Characterization of Modified Nanoparticles

The x-ray diffraction (XRD), shown in Figure 3.5 A), was used to determine the composition of the materials, the Miller indices found to show the presence of six characteristic peaks for the typical cubic structure of Fe$_3$O$_4$: (220), (311), (400), (422), (511), (204) (according to JCPDS 19-629) confirming the formation of magnetite.[21a] For the Fe$_3$O$_4$@TiO$_2$ the Miller indices of magnetite remained however new indices characteristic for TiO$_2$ anatase phase (101), (004), (200), (105), (211), (115), (220), (215) (according to JCPDS 21-1272) were observed indicating that the surface of the

nanoparticles had become coated. The shape and particles size of the Fe_3O_4 and $Fe_3O_4@TiO_2$ were investigated using scanning electron microscopy (SEM), the images are shown in Figure 3.5 B) and C). Both the Fe_3O_4 and $Fe_3O_4@TiO_2$ had a size of around 200 nm. Energy-dispersive X-ray spectroscopy (EDX) and elemental mapping, shown in Appendix Eighteen, was measured to investigate the surface composition. The elemental mapping analysis carried out at randomly selected areas of the sample shows the expected elements, namely Fe and Ti. It also showed the distribution of Ti coating on the surface of Fe_3O_4 to be fairly uniform.
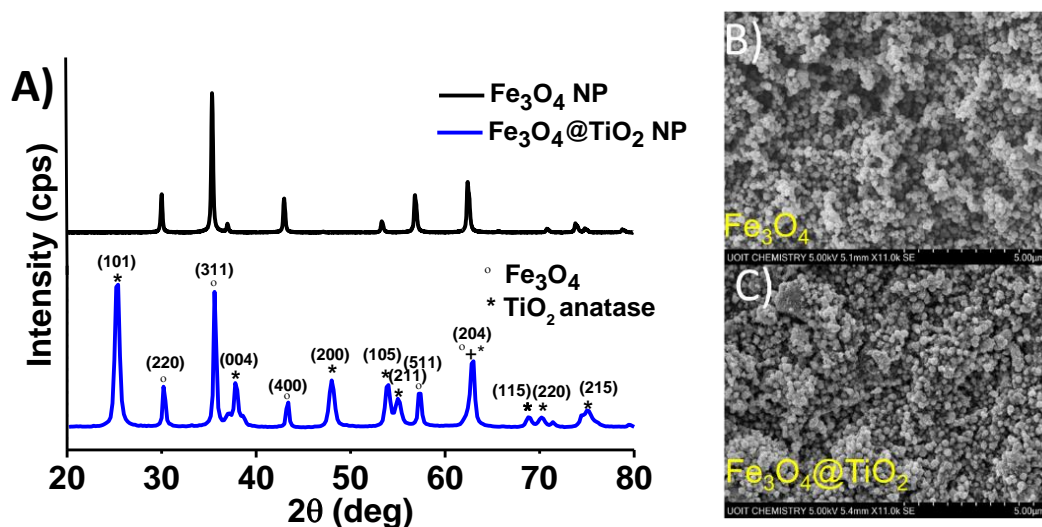
Figure 3.5 A) XRD of Fe₃O₄ and Fe₃O₄@TiO₂ B) SEM image of Fe₃O₄ C) SEM image of Fe₃O₄@TiO₂

To understand the surface area and porosity of the Fe_3O_4 NP and $Fe_3O_4@TiO_2$ NP the N_2 adsorption isotherms were measured for both materials, shown in Appendix Seventeen. The isotherm for the Fe_3O_4 NP showed no hysteresis, however, the isotherm for the $Fe_3O_4@TiO_2$ did. This is promising because hysteresis is an indication of a mesoporous material and a common mesoporous metal oxide is titanium oxide. The BET surface area

of the Fe_3O_4 was calculated to be 11.2 m^2/g and the average pore radius is 2.10 nm. The BET surface area of the $Fe_3O_4@TiO_2$ was calculated to be 58.3 m^2/g and the average pore radius is 2.14 nm. The increased surface area of the coated nanoparticles is advantageous because it offers more area for L to bind onto.

One of the main advantages of using magnetite is to gain the magnetic characteristics giving the materials recyclable potential. A visual representation of how Fe_3O_4 and $Fe_3O_4@TiO_2$ respond to a magnet is shown in Appendix Sixteen. The Fe_3O_4 material is pulled from the solution very quickly when the magnet was near. The $Fe_3O_4@TiO_2$ took longer to be pulled from the solution when the magnet was near, probably due to the coating of the non-magnetic TiO_2 layer on the surface. Both materials are attracted to the magnet, showing their ability to be recycled from the solution. Importantly, after the magnetic field was removed both materials could be effectively re-dispersed in the media.

It should also be noted that the two materials have different colors, upon coating with TiO_2 the Fe_3O_4, the TiO_2 coating changes the color of the microspheres from a black color to burgundy. This color change is a good indication that the surface has been coated with a TiO_2 layer. To evaluate the magnetic characteristics of $L-Fe_3O_4@TiO_2$, the magnetic hysteresis loop was measured and compared to the magnetic hysteresis loop of $Fe_3O_4@TiO_2$. The magnetic hysteresis loops at T = 300K, for both materials are shown in Figure 3.6, it also shows a photo of $L-Fe_3O_4@TiO_2$ being pulled from solution using a magnet. As shown in the hysteresis loop there is no change to the magnetic properties due to the coating with L, the magnetic saturation (M_S) for both $L-Fe_3O_4@TiO_2$ and $Fe_3O_4@TiO_2$ were determined to be ±70 emu/g. This shows that $L-Fe_3O_4@TiO_2$ has good potential as a recyclable Hg^{2+} sensor/uptake system.

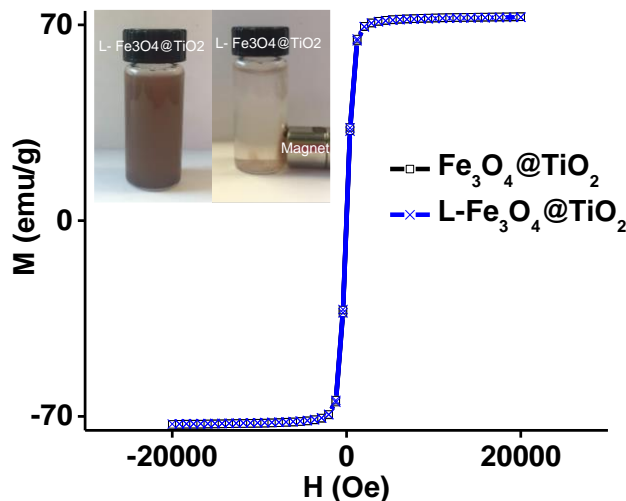*Figure 3.6 Magnetic hysteresis curves of Fe₃O₄@TiO₂ and L-Fe₃O₄@TiO₂ microspheres; photo of L-Fe₃O₄@TiO₂ before and after magnetic separation*

To confirm the presence of L on the surface of L-Fe$_3$O$_4$@TiO$_2$ the thermogravimetric analysis (TGA) and differential thermal analysis (DTG) of the materials were measured under air and argon atmospheres then compared to the TGA and DTG of the bare Fe$_3$O$_4$@TiO$_2$. In the TGA of the bare Fe$_3$O$_4$@TiO$_2$, shown in Figure 3.7 A), water is seen to evaporate off around 100°C. In the TGA of the L-Fe$_3$O$_4$@TiO$_2$ shown in Figure 3.7 B), there are two mass loss peaks. The mass loss of 2.5% around 360°C is indicative of L being burned off the surface, which was confirmed by measuring the TGA and DTG of L alone, shown in Appendix Fifteen. The DTG of L-Fe$_3$O$_4$@TiO$_2$ showed multiple peaks, the first peak around 360°C which again is indicative of L, this peak is very broad in when measured under air; however, when measured under argon two distinct peaks appear. This difference between the DTG may be due to combustion occurring while L is decomposing in air. In conclusion, the TGA and DTG showed peaks for L as well as the siloxane template supporting that L has been functionalized onto the surface.
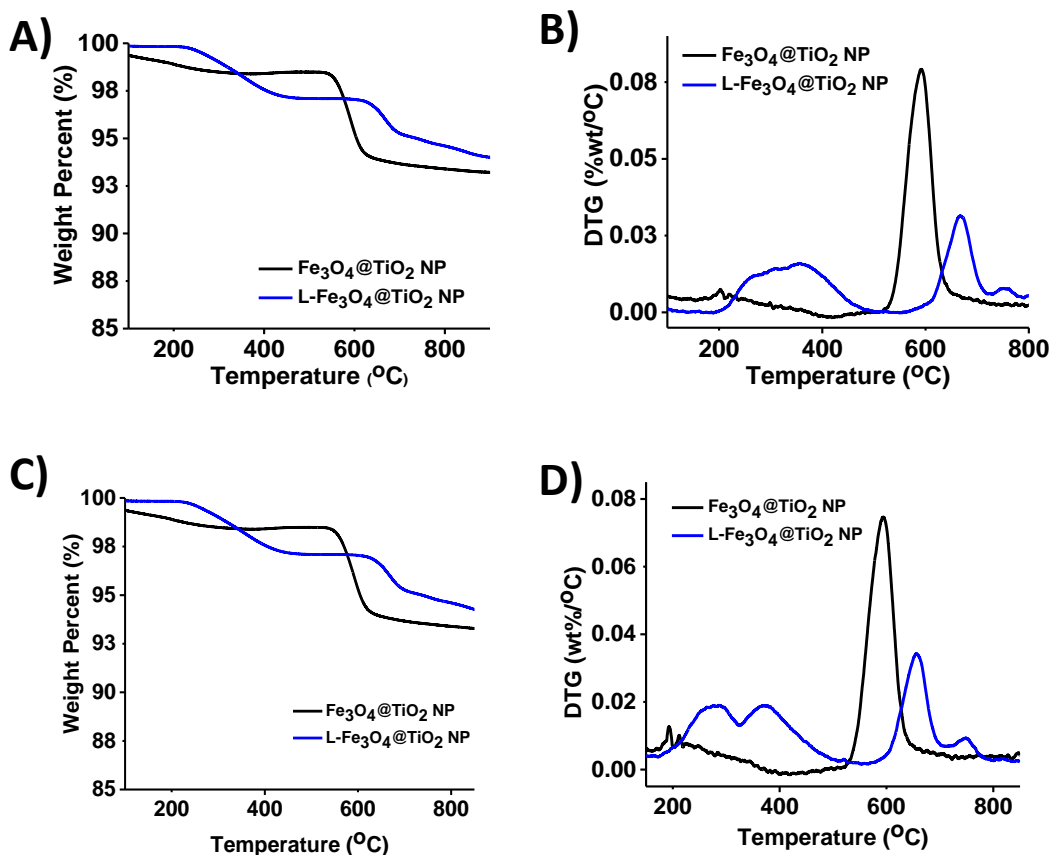
Figure 3.7 **A)** *TGA analysis of $Fe_3O_4@TiO_2$ and L-$Fe_3O_4@TiO_2$ and* **B)** *DTG analysis of $Fe_3O_4@TiO_2$ and L-$Fe_3O_4@TiO_2$ under Air* **C)** *TGA analysis of $Fe_3O_4@TiO_2$ and L-$Fe_3O_4@TiO_2$ and* **D)** *DTG analysis of $Fe_3O_4@TiO_2$ and L-$Fe_3O_4@TiO_2$ under Argon*

3.4 Sensing on the Surface of the L-$Fe_3O_4@TiO_2$

Sensitivity fluorescence spectra of L-$Fe_3O_4@TiO_2$ was run at a lower excitation of λ_{exc} = 330 nm, when a high excitation of λ_{exc} = 380 nm is used the emission peaks for TiO_2 become too predominate and overshadow the L emission peak.[31] The peak intensity of L has decreased greatly due to the silane template method of the pyridine, this is due to the quaternization of the pyridine tail in L. When the pyridine becomes quaternized a halide anion is required to balance the positive charge on the nitrogen. Halide anions are known to act as quenching agents,[32] the effect of halide quenching in shown in Appendix

Fourteen for QL in solution. The sensitivity of L-Fe$_3$O$_4$@TiO$_2$ was determined by introducing Hg^{2+} and measuring the fluorescence spectra (Figure 3.8 A) and B)). Since L-Fe$_3$O$_4$@TiO$_2$ is expected to act as a "turn-off" fluorescence sensor at the peak around 413 nm which is indicative of L, the peak should quench as the concentration of Hg^{2+} increases. The peak around 413 nm does quench linearly in the range of 2.7 ppm to 6.5 ppm, the linear regression of these points on the calibration graph has an $R^2 = 0.935$ and a standard deviation of 0.094. The LOD can be seen in the calibration graph, it is clear that the lowest concentration of Hg^{2+} that can be reliably detected by the fluorescence is 2.7 ppm. Showing that L could be embedded onto the surface and act as a sensor; however, further improvements to the system to improve the signal are required.
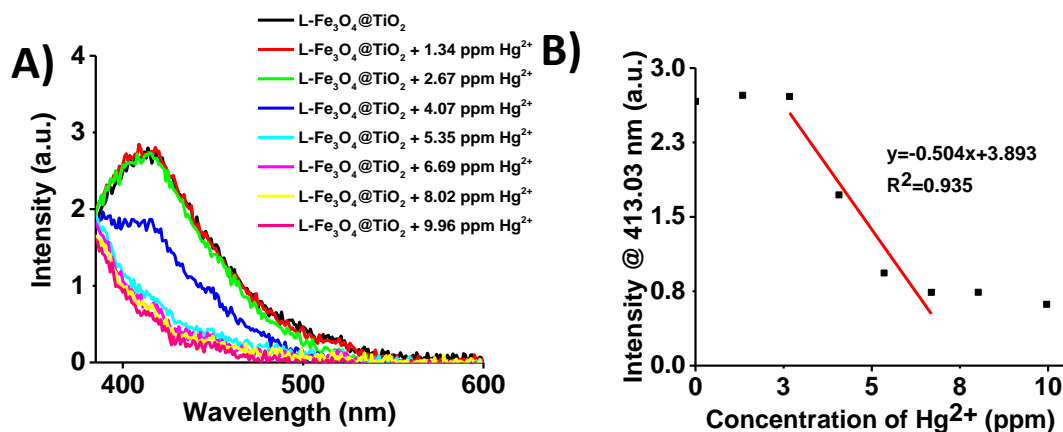
*Figure 3.8 **A**) Fluorescence Spectra of L-Fe$_3$O$_4$@TiO$_2$ with the addition of Hg^{2+} in ACN **B**) Calibration curve for peak intensity @ 413nm in ACN*

The XPS analysis, shown in Figure 13, of Hg^{2+}-L-Fe$_3$O$_4$@TiO$_2$ is not a simple task. The most intense mercury (Hg 4f) peaks overlap with the most intense peak of silicon (Si 2p). Peak deconvolution is possible (Figure 3.9 H) if fixing a full width at half-maximum (fwhm) of Si 2p peak at the same level as Si 2p peak of a blank L-Fe$_3$O$_4$@TiO$_2$ material

(Figure 3.9 G). Peak area normalization between N 1s and Hg 4f using relative XPS sensitivity factors as determined by Schofield[41] gives an N/Hg ratio equal to 2.0:0.38. This suggests that in this case, only 38% of ligand molecules form the complex. The complex formation is also confirmed by the splitting of the S 2s peak. The S 2s peak of L-Fe_3O_4@TiO_2 is centered at 227.5 eV, which is characteristic to S2- in thio-organic compounds. When the material is reacted with mercury, a new S2s peak at 232.3 eV appears demonstrating that the electron density is withdrawn from sulfur perhaps through the σ-bonding to complexed mercury. The ratio of the newly formed to the initial S 2s peak is 1.0:1.6, which gives 37% of sulfur involved in the complex formation. The XPS area of N 1s contains 2 peaks: one corresponding to a nitrogen atom in the chelating bis-thienylpyridine moiety at 399.3 eV and the second one is characteristic to N+ of the anchoring pyridyl unit at 401.6 eV. Interestingly, the complex formation has a minor influence on the positions of N1s peaks. Finally, the appearance of the secondary mercury line (Hg 4d) signals that are not overlapping with any of the materials elements (Figure 3.9 D) directly demonstrates mercury uptake and formation of Hg^{2+}-L-Fe_3O_4@TiO_2.
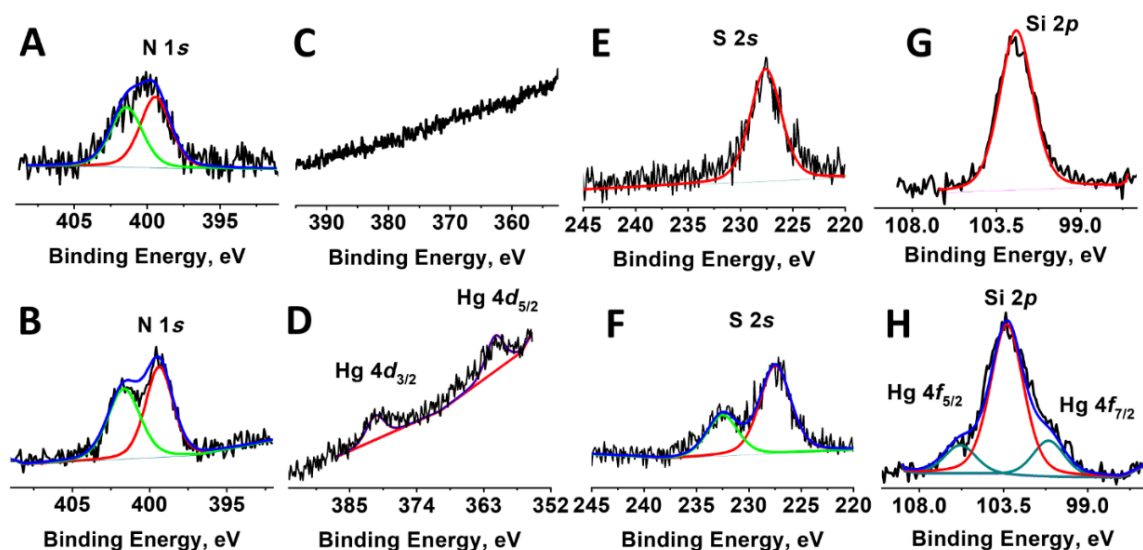
Figure 3.9 X-ray photoelectron spectra of L-Fe$_3$O$_4$@TiO$_2$ (upper row A, C, E, G) and Hg^{2+}-L-Fe$_3$O$_4$@TiO$_2$ (down row B, D, F, H) showing corresponding N1s, Hg 4d, S2s, and Si2p/ Hg 4f, areas. The black line shows the experimental data, while the red, blue or green lines are the overall fitted spectra. The Si 2p peak for the Hg^{2+}-L-Fe$_3$O$_4$@TiO$_2$ has been deconvoluted: the red line represent the silicon from the silane template, the light-blue line correspond to the Hg^{2+}

In order to determine the selectivity of L-Fe$_3$O$_4$@TiO$_2$ the fluorescence spectra are measured in the presence of other transition metals (Cr^{3+}, Zn^{2+}, Fe$^{3+/2+}$, Co^{2+}, Ru^{3+}, Cd^{2+}, Cu^{2+}) before the addition of Hg^{2+} again. As before, this was done to not only determine the selectivity of the material but to also evaluate which metal complexes are preferentially formed. A bar graph depicting the selectivity for the fluorescence signal is shown in Figure 14 for L-Fe$_3$O$_4$@TiO$_2$. Similar to L, the only major interference comes from Fe^{3+} ions. Other soft metals such as Zn^{2+} and Cd^{2+} ions do not interfere greatly. The slight differences in selectivity of the material compared to L could be explained by significant changes in electronics of L upon quaternization step performed to anchor the molecule to the chlorobenzylsiloxane pre-modified surface, as previously reported for other ligand

architectures.[16b] Showing L-Fe_3O_4@TiO_2 is fairly selective for Hg^{2+} with only interference from Fe^{3+} ions.

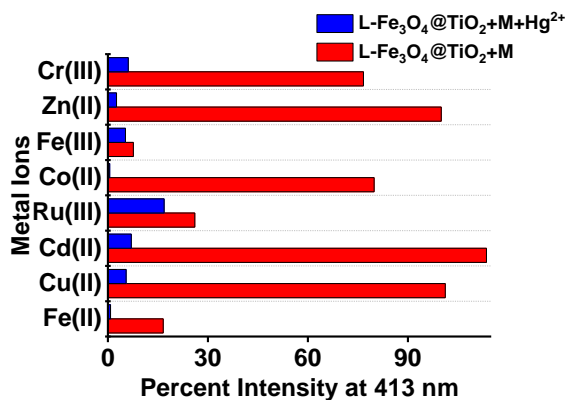*Figure 3.10 The selectivity of L-Fe_3O_4@TiO_2 in the presence of several transition metals (Cr^{3+}, Zn^{2+}, $Fe^{3+/2+}$, Co^{2+}, Ru^{3+}, Cd^{2+}, Cu^{2+})*

4 Conclusions and Future Work

In conclusion, the Hg^{2+}-L complex was successfully synthesized and the structure (SNS mode of coordination was confirmed using UV-vis and several NMR techniques such as ^{1}H-NMR, ^{13}C{H}-NMR, ^{1}H-^{1}H COSY-NMR, ^{1}H-^{13}C HMBC-NMR, ^{1}H-^{13}C HSQC-NMR and DEPT135. The ^{1}H-NMR showed is a significant downfield shift for characteristic doublets corresponding to non-chelating pyridine ring from 8.78 and 8.04 ppm in the free ligand to 8.90 and 8.49 ppm, respectively. In addition, singlet resonance at 8.22 ppm of the protons of chelating pyridine ring and doublet resonance at 8.07 ppm for the thiophene protons had become noticeably shifted up field. The structure of the Hg^{2+}-L complex was also confirmed using ^{13}C{H}-NMR, it showed seven peaks of the possible ten carbon peaks in L. Quaternary carbons were not well resolved and were located and assigned with the help of ^{1}H-^{13}C-HMBC NMR.

The potential for L to be a fluorescent sensor for Hg^{2+} was investigated in solution first, when using an emission wavelength of 380 nm L showed a strong characteristic fluorescence emission signal at 413 nm; however, this signal was quenched linearly when Hg^{2+} was introduced and a new fluorescence emission signal at 563 nm corresponding to Hg^{2+}-L increased linearly. This red shift of the emission peaks could be seen in both the fluorescence spectra as well as visually. Free L in solution fluorescence in the blue region, once Hg^{2+}-L was formed the solution emitted in the yellow region. The one isosbestic point at 500 nm in the fluorescent spectra supports the idea that L is going to Hg^{2+}-L without forming any intermediates. The LOD determined for both calibration curves was determined to be 1.4 ppm of Hg^{2+}. The selectivity of L for Hg^{2+} was also determined, showing that L can effectively detect Hg^{2+} as well as differentiate competing Zn^{2+}, Cd^{2+}, Cu^{2+}, Co^{2+}, Cr^{3+}, Ru^{3+}, Fe^{2+} ions in solution. While many of these completing ions caused some quenching of the peak at 413 nm none of them produced a strong emission signal at 563 nm. The only major interference came from Fe^{3+} which quenched the 413 nm peak and produced a peak at 563 nm comparative to Hg^{2+}-L. This support the idea of the L as an efficient turn on/off fluorescent sensor for Hg^{2+} ion.

The Fe_3O_4 and Fe_3O_4@TiO_2 microspheres were successfully synthesized and characterized using SEM, XRD and BET. The SEM showed that both coated and uncoated microspheres were in average 200 nm in size. While Fe_3O_4 particles looked smooth on the surface the Fe_3O_4@TiO_2 had a coarser surface indicating the particles have been coated as judged by SEM. The XRD of the Fe_3O_4 showed that all the Miller indices were consistent with the reported Miller indices for magnetite. The XRD of Fe_3O_4@TiO_2 showed the addition of Miller indices for TiO_2 anatase indicating the magnetite surface had been coated

with TiO_2. The BET analysis of Fe_3O_4 and $Fe_3O_4@TiO_2$ showed that $Fe_3O_4@TiO_2$ were mesoporous and had a much larger surface area than Fe_3O_4 (11.2 vs 58.3 m^2/g, respectively). Upon placing a magnet near Fe_3O_4 and $Fe_3O_4@TiO_2$, the material would move towards the magnet showing promising removal properties. It was possible to attach L onto the surface of the $Fe_3O_4@TiO_2$ through a silane linker. This material was characterized using TGA and XPS, which showed a 1:1 N/N^+ ratio on the surface as expected. The TGA showed a mass loss of 2.5% around 360^oC which is indicative of L being burned off the surface. This confirms that $L-Fe_3O_4@TiO_2$ had been successfully synthesized.

The emission of $L-Fe_3O_4@TiO_2$ was measured a lower excitation wavelength (325 nm). The decrease of the intensity of the peak at 413 nm could be explained by the surface functionalization by the quaternization of L onto the siloxane template. The peak of 413 nm was quenching linearly as the concentration of Hg^{2+} increased. The $L-Fe_3O_4@TiO_2$ was able to sense Hg^{2+} from 2.8 ppm to 6.5 ppm with an $R^2 = 0.935$ and a LOD = 2.67 ppm. The $L-Fe_3O_4@TiO_2$ was seen to be very selective for Hg^{2+} against several transition metals (Cr^{3+}, Zn^{2+}, Co^{2+}, Ru^{3+}, Cd^{2+}, and Cu^{2+}). The only major interference came from Fe^{3+}, which significantly quenched the 413 nm emission peak. The slight differences in selectivity of the material compared to L could be explained again by the significant changes in electronics of L upon quaternization step performed to anchor the molecule. The $L-Fe_3O_4@TiO_2$ was shown to have great potential as an Hg^{2+} sensor and uptake system.

In the future, the knowledge obtained as part of this research could be used for the development of novel magnetic materials for the detection and uptake of toxic metals. A

major obstacle was the microsphere size interfering with the spectroscopic sensing/ analysis. It may use a different method reported by Obaidat[33] for the synthesis of $Fe_3O_4@TiO_2$ nanosurfaces that are less than 100 nm in size. Alternatively, the same coating method used in the work could be applied to a smaller Fe_3O_4 core. The coating mechanism assumes that the positively charged ammonia ions are attracted to the negatively charged carboxyl groups in the Fe_3O_4 surface, the negatively charged TiO^- species are attracted to the ammonia ions then through a surface condensation reaction the surface becomes coated in TiO_2. By using a smaller core with a similar negative surface charge smaller $Fe_3O_4@TiO_2$ materials could be obtained. Future directions also include the synthesis of the ligand with a phenol tail as oppose to a pyridine tail, this could be able to functionalize onto the silane template through a C-O-C bond as opposed to a quarternized nitrogen; therefore, improving the intensity of the emission signal of the ligand on the surface.

5 Bibliography

[1] a) M. L. Mallory, J. F. Provencher, G. J. Robertson, B. M. Braune, E. R. Holland, S. Klapstein, K. Stevens and N. J. O'Driscoll, *Ecotoxicol Environ Saf* **2018**, *157*, 424-430; b) R. A. Lavoie and L. M. Campbell, *Arch Environ Contam Toxicol* **2018**, *75*, 111-120; c) B. L. Reinhart, K. A. Kidd, R. A. Curry, N. J. O'Driscoll and S. A. Pavey, *J Environ Sci (China)* **2018**, *68*, 41-54; d) S. M. Crowley, D. P. Hodder, C. J. Johnson and D. Yates, *Ecol. Indic.* **2018**, *89*, 63-73.

[2] M. R. Neff, S. P. Bhavsar, G. B. Arhonditsis, R. Fletcher and D. A. Jackson, *J Environ Monit* **2012**, *14*, 2327-2337.

[3] a) J. Plotka-Wasylka, M. Rutkowska, B. Cieslik, A. Tyburcy and J. Namiesnik, *J Anal Methods Chem* **2017**, *2017*, 5283917; b) F. Ruggieri, C. Majorani, F. Domanico and A. Alimonti, *Int J Environ Res Public Health* **2017**, *14*; c) B. Mondal, D. Maulik, M. Mandal, G. N. Sarkar, S. Sengupta and D. Ghosh, *J Gastrointest Cancer* **2017**, *48*, 361-368.

[4] a) B. D. Barst, M. Rosabal, P. E. Drevnick, P. G. C. Campbell and N. Basu, *Environ Pollut* **2018**, *242*, 63-72; b) A. Vahidinia, F. Samiee, J. Faradmal, A. Rahmani, M. Taravati Javad and M. Leili, *Biol Trace Elem Res* **2018**; c) L. Dix-Cooper and T. Kosatsky, *Sci Total Environ* **2018**, *619-620*, 1409-1419.

[5] a) S. T. Palisoc, D. J. S. Uy, M. T. Natividad and T. B. G. Lopez, *Mater Res Express* **2017**, *4*; b) A. Giacomino, A. Ruo Redda, S. Squadrone, M. Rizzi, M. C. Abete, C. La Gioia, R. Toniolo, O. Abollino and M. Malandrino, *Food Chem* **2017**, *221*, 737-745.

[6] a) J.-F. Chen, X.-B. Cheng, H. Li, B.-B. Han, Q. Lin, Y.-M. Zhang, H. Yao and T.-B. Wei, *New J. Chem.* **2017**, *41*, 12707-12712; b) S. Zhu, L. He, F. Zhang, M. Li, S. Jiao, Y. Li, M. Chen, X. E. Zhao and H. Wang, *Talanta* **2016**, *161*, 769-774.

[7] a) N. Kaur, *Synth. Commun.* **2018**, *48*, 2715-2749; b) B. Giese, *Angew. Chem.* **1985**, *24*, 553-565; c) G. Dyker, *Angew. Chem.* **1999**, *38*, 1698-1712.

[8] R. G. Pearson, *JACS* **1963**, *85*, 3533-3539.

[9] H. Lv, Z. Ren, H. Liu, G. Zhang, H. He, X. Zhang and S. Wang, *Tetrahedron* **2018**, *74*, 1668-1680.

[10] a) F. Zapata, A. Caballero, A. Espinosa, A. Tárraga and P. Molina, *JOC* **2009**, *74*, 4787-4796; b) F. Zapata, A. Caballero, P. Molina and A. Tarraga, *Sensors (Basel)* **2010**, *10*, 11311-11321; c) G. Li, X. Ren, G. Shan, W. Che, D. Zhu, L. Yan, Z. Su and M. R. Bryce, *Chem Commun (Camb)* **2015**, *51*, 13036-13039; d) M. T. Gabr and F. C. Pigge, *Dalton Trans* **2018**, *47*, 2079-2085; e) T. Liu, K. Liu, J. Zhang and Z. Wang, *ChemistrySelect* **2018**, *3*, 5559-5565; f) D. Saccone, C. Magistris, N. Barbero, P. Quagliotto, C. Barolo and G. Viscardi, *Materials* **2016**, *9*, 137.

[11] A. K. Shigemoto, C. N. Virca, S. J. Underwood, L. R. Shetterly and T. M. McCormick, *J. Coord. Chem.* **2016**, *69*, 2081-2089.

[12] a) S. R. Bhatta, B. Mondal, G. Vijaykumar and A. Thakur, *Inorg. Chem.* **2017**, *56*, 11577-11590; b) N. I. Georgiev, M. D. Dimitrova, Y. D. Todorova and V. B. Bojinov, *Dyes and Pigments* **2016**, *131*, 9-17.

[13] D. Udhayakumari, S. Suganya, S. Velmathi and D. MubarakAli, *Journal of Molecular Recognition* **2014**, *27*, 151-159.

[14] a) H. Wang, Y. Wang, J. Jin and R. Yang, *Anal. Chem.* **2008**, *80*, 9021-9028; b) Y. Ding, S. Wang, J. Li and L. Chen, *TrAC Trends in Analytical Chemistry* **2016**, *82*, 175-190; c) K. M. M. Kabir, S. J. Ippolito, A. E. Kandjani, Y. M. Sabri and S. K. Bhargava, *TrAC Trends in Analytical Chemistry* **2017**, *88*, 77-99; d) S. Botasini, G. Heijo and E. Mendez, *Anal Chim Acta* **2013**, *800*, 1-11.

[15] a) N. Wu, Y. Tang, M. Zeng, J. Gao, X. Lu and Y. Zheng, *J. Lumin.* **2018**, *202*, 502-507; b) L. Motiei, M. Altman, T. Gupta, F. Lupo, A. Gulino, G. Evmenenko, P. Dutta and M. E. van der Boom, *Journal of the American Chemical Society* **2008**, *130*, 8913-8915.

[16] a) N. O. Laschuk, I. I. Ebralidze, S. Quaranta, S. T. W. Kerr, J. G. Egan, S. Gillis, F. Gaspari, A. Latini and O. V. Zenkina, *Mater. Des.* **2016**, *107*, 18-25; b) J. T. S. Allan, S. Quaranta, Ebralidze, II, J. G. Egan, J. Poisson, N. O. Laschuk, F. Gaspari, E. B. Easton and O. V. Zenkina, *ACS Appl Mater Interfaces* **2017**, *9*, 40438-40445.

[17] K. T. Kim, S. A. Yoon, J. Ahn, Y. Choi, M. H. Lee, J. H. Jung and J. Park, *Sens. Actuators B-Chem.* **2017**, *243*, 1034-1041.

[18] T. Placido, G. Aragay, J. Pons, R. Comparelli, M. L. Curri and A. Merkoçi, *ACS Appl. Mater. Interfaces* **2013**, *5*, 1084-1092.

[19] N. Vasimalai, G. Sheeba and S. A. John, *J Hazard Mater* **2012**, *213-214*, 193-199.

[20] a) A. K. Gupta and M. Gupta, *Biomaterials* **2005**, *26*, 3995-4021; b) P. Xu, G. M. Zeng, D. L. Huang, C. L. Feng, S. Hu, M. H. Zhao, C. Lai, Z. Wei, C. Huang, G. X. Xie and Z. F. Liu, *Sci Total Environ* **2012**, *424*, 1-10; c) R. Hudson, Y. Feng, R. S. Varma and A. Moores, *Green Chem.* **2014**, *16*, 4493-4505.

[21] a) T. Xin, M. Ma, H. Zhang, J. Gu, S. Wang, M. Liu and Q. Zhang, *Appl Surf Sci.* **2014**, *288*, 51-59; b) Z.-D. Li, H.-L. Wang, X.-N. Wei, X.-Y. Liu, Y.-F. Yang and W.-F. Jiang, *J Alloys Compd* **2016**, *659*, 240-247; c) W.-F. Ma, Y. Zhang, L.-L. Li, L.-J. You, P. Zhang, Y.-T. Zhang, J.-M. Li, M. Yu, J. Guo, H.-J. Lu and C.-C. Wang, *ACS Nano* **2012**, *6*, 3179-3188; d) P. I. Girginova, A. L. Daniel-da-Silva, C. B. Lopes, P. Figueira, M. Otero, V. S. Amaral, E. Pereira and T. Trindade, *J Colloid Interface Sci* **2010**, *345*, 234-240.

[22] K. Rurack, **2008**, *5*, 101-145.

[23] A. T. R. Williams, S. A. Winfield and J. N. Miller, *Analyst* **1983**, *108*, 1067-1071.

[24] H. Deng, X. Li, Q. Peng, X. Wang, J. Chen and Y. Li, *Angew. Chem.* **2005**, *117*, 2842-2845.

[25] J. Yu, Y. Su, B. Cheng and M. Zhou, *J. Mol. Catal. Chem.* **2006**, *258*, 104-112.

[26] a) S. Yitzchaik and T. J. Marks, *Accounts of Chemical Research* **1996**, *29*, 197-202; b) J. Choudhury, R. Kaminker, L. Motiei, G. d. Ruiter, M. Morozov, F. Lupo, A. Gulino and M. E. v. d. Boom, *Journal of the American Chemical Society* **2010**, *132*, 9295-9297.

[27] a) P. Singla, P. Kaur and K. Singh, *Sens. Actuators B-Chem.* **2017**, *244*, 299-306; b) S. Sarkar, S. Roy, R. N. Saha and S. S. Panja, *J Fluoresc* **2018**, *28*, 427-437.

[28] a) E. Babu, P. Muthu Mareeswaran, S. Singaravadivel, J. Bhuvaneswari and S. Rajagopal, *Spectrochim Acta A Mol Biomol Spectrosc* **2014**, *130*, 553-560; b) Y. Cui, Y. Hao, Y. Zhang, B. Liu, X. Zhu, P. Qu, D. Li and M. Xu, *Spectrochim Acta A Mol Biomol Spectrosc* **2016**, *165*, 150-154.

[29] E. R. Monazam, R. W. Breault and R. Siriwardane, *Industrial & Engineering Chemistry Research* **2014**, *53*, 13320-13328.

[30] W.-J. Wu, J. Wang, M. Chen, D.-J. Qian and M. Liu, *J. Phys. Chem. C* **2017**, *121*, 2234-2242.

[31] S. Mathew, A. K. Prasad, T. Benoy, P. P. Rakesh, M. Hari, T. M. Libish, P. Radhakrishnan, V. P. Nampoori and C. P. Vallabhan, *J Fluoresc* **2012**, *22*, 1563-1569.

[32] J. R. Lakowicz, *Principles of fluorescence spectroscopy*, Second edition. New York : Kluwer Academic/Plenum, [1999] ©1999, **1999**, p.

[33] S. Khashan, S. Dagher, N. Tit, A. Alazzam and I. Obaidat, *Surf Coat Technol.* **2017**, *322*, 92-98.

6 Appendix
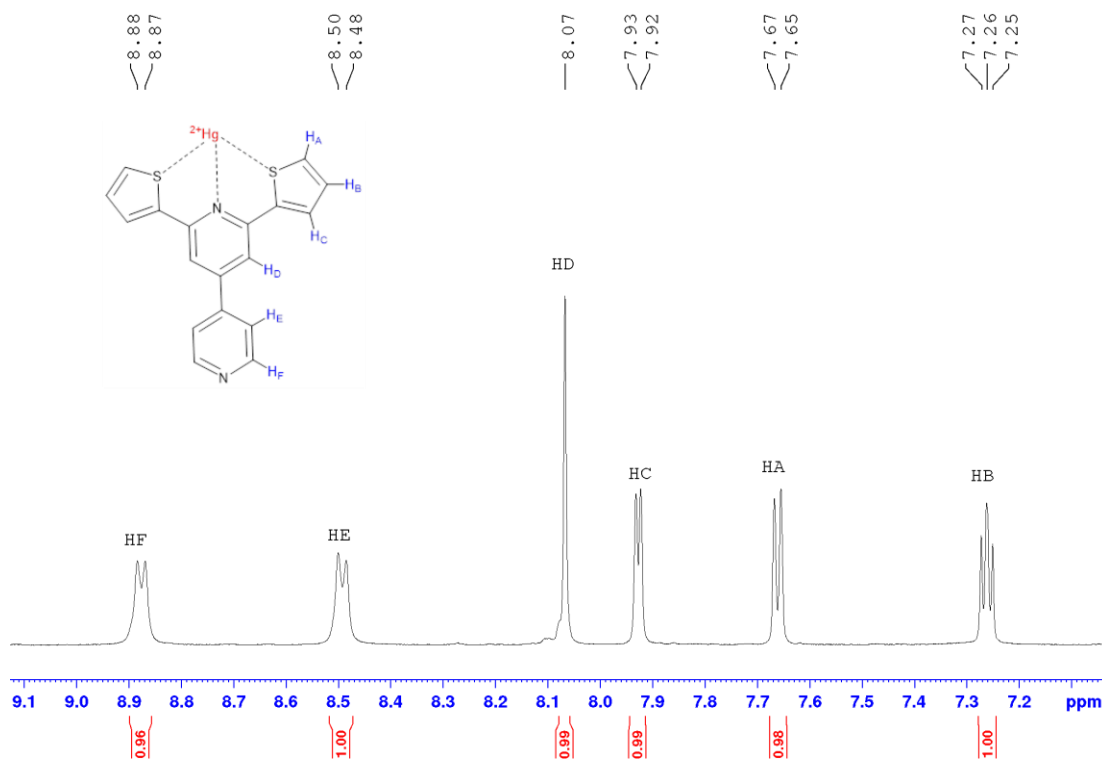
Appendix One: ^{1}H-NMR of Hg^{2+}-L
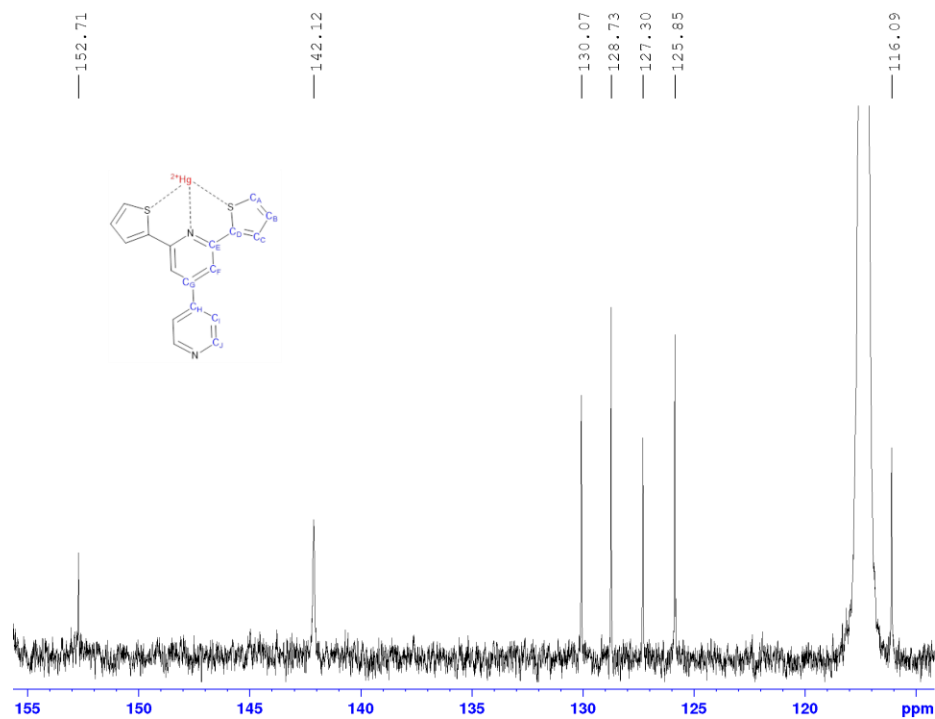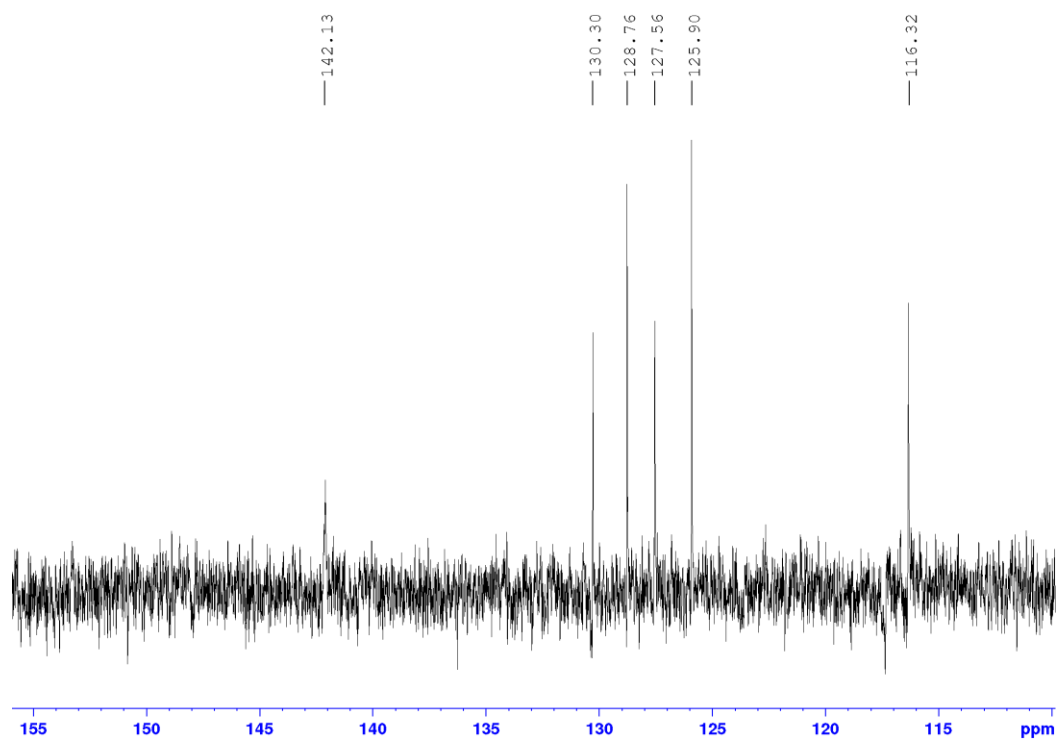

Appendix Two: ^{13}C{H}-NMR of Hg^{2+}-L
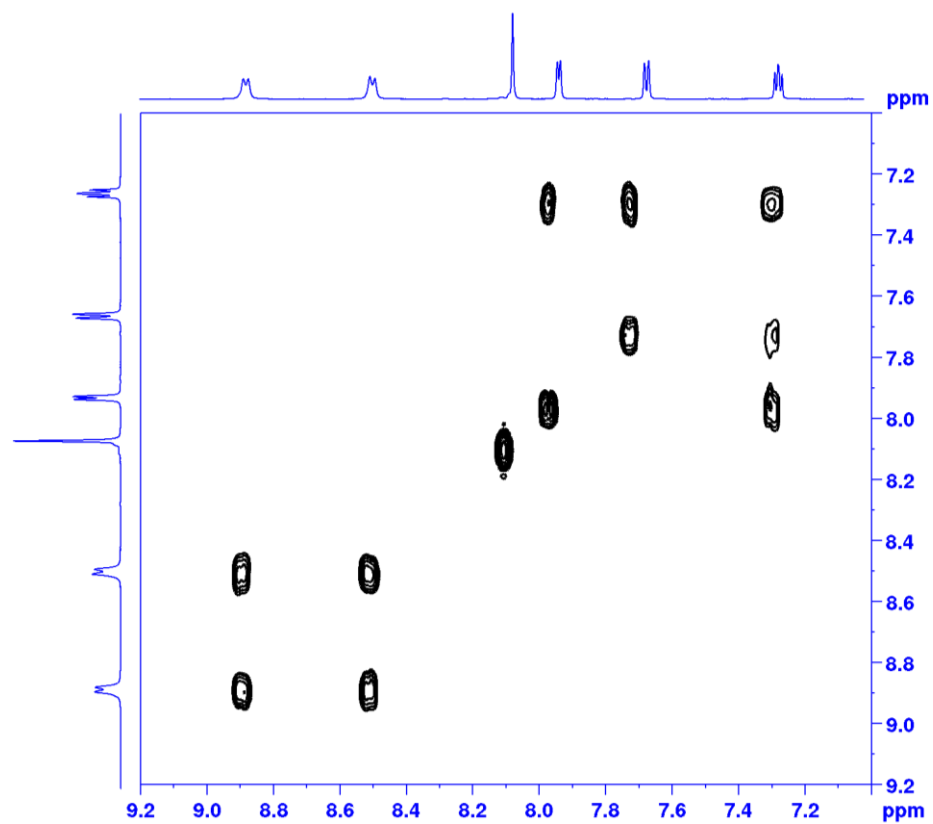
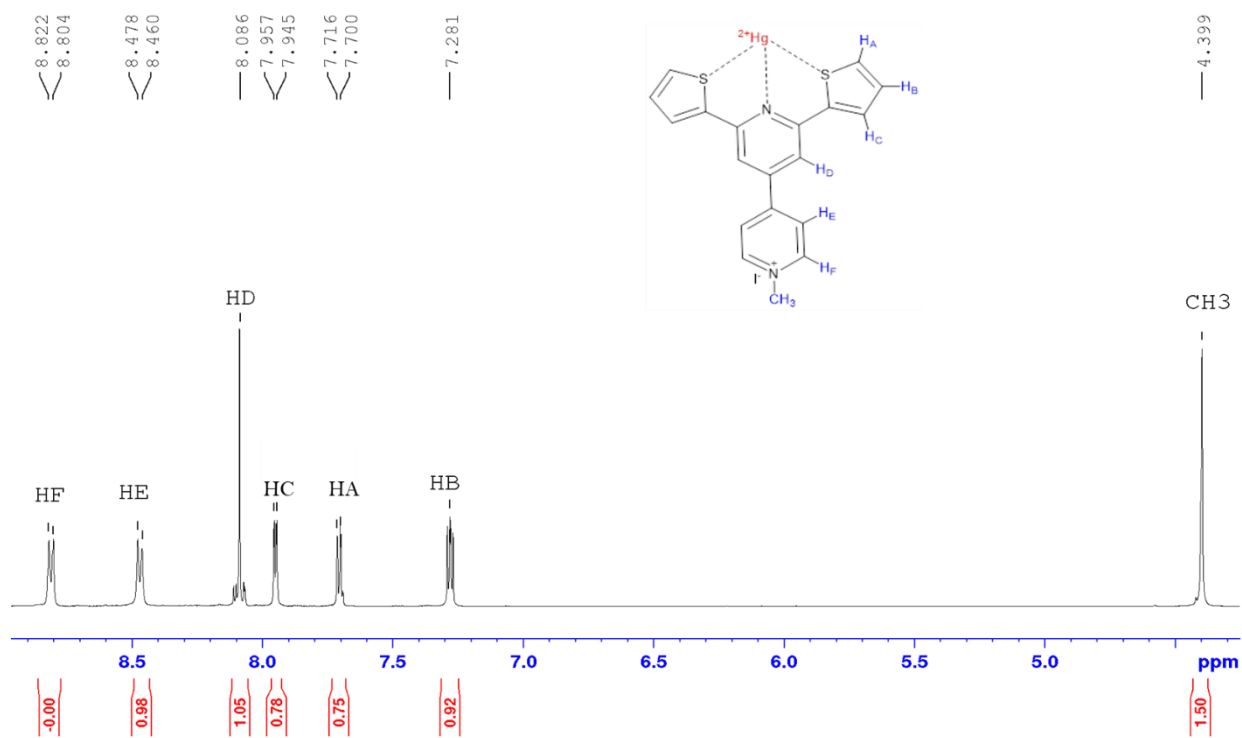Appendix Three: ^{1}H-^{1}H COSY-NMR of Hg^{2+}-L
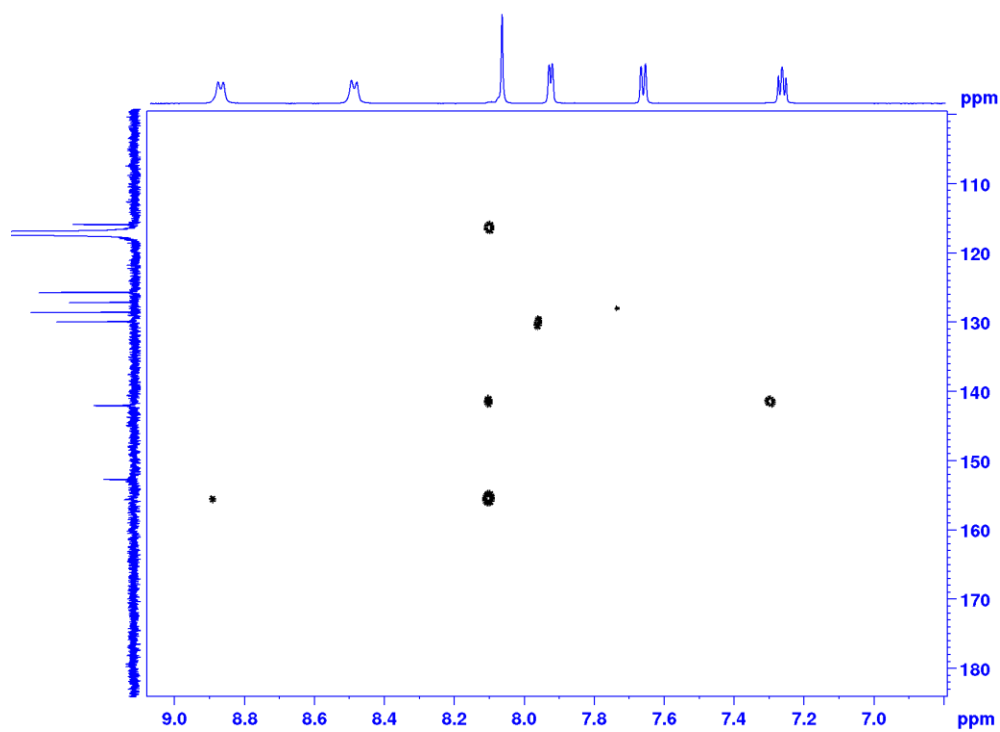
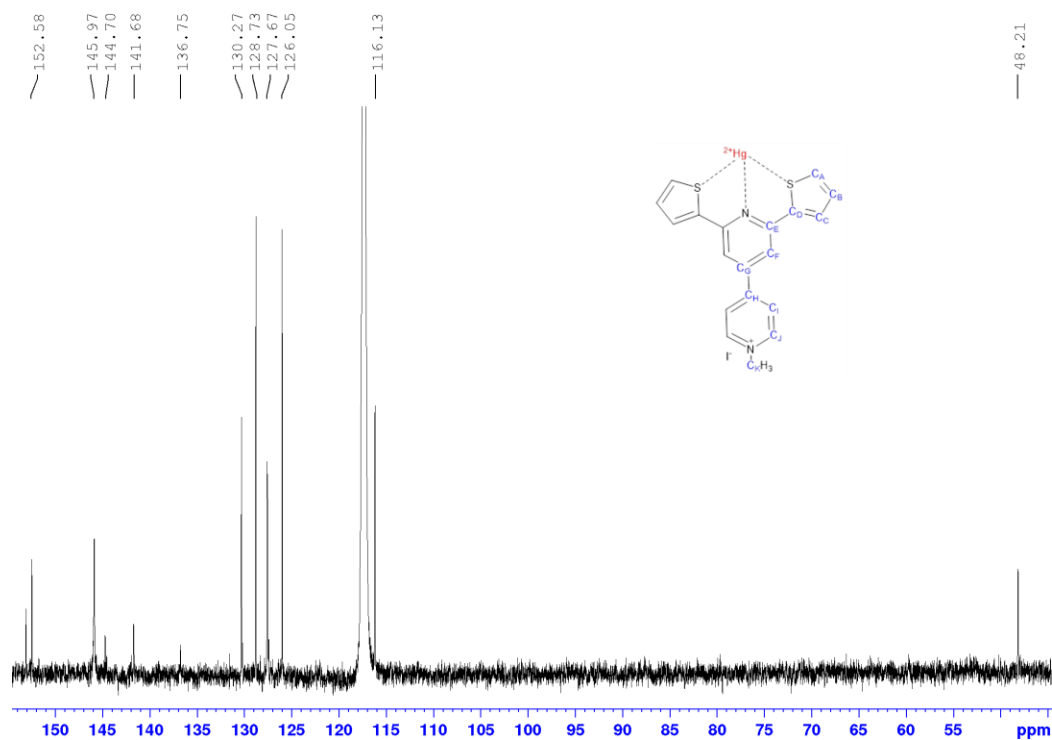Appendix Four: ^{1}H-^{13}C HMBC-NMR of Hg^{2+}-L
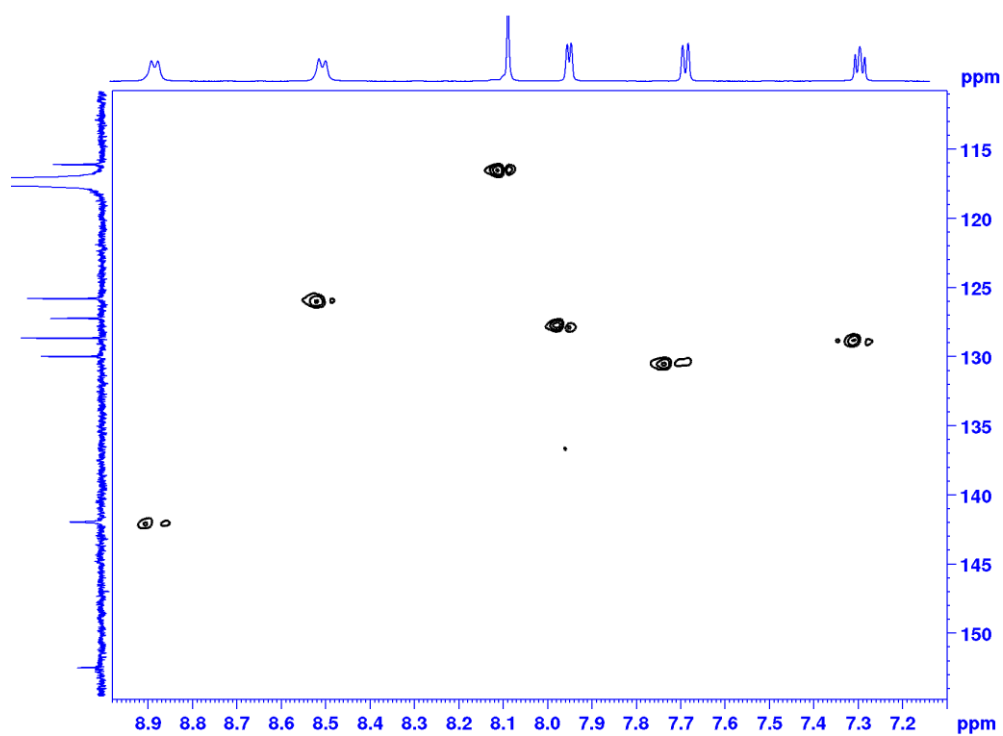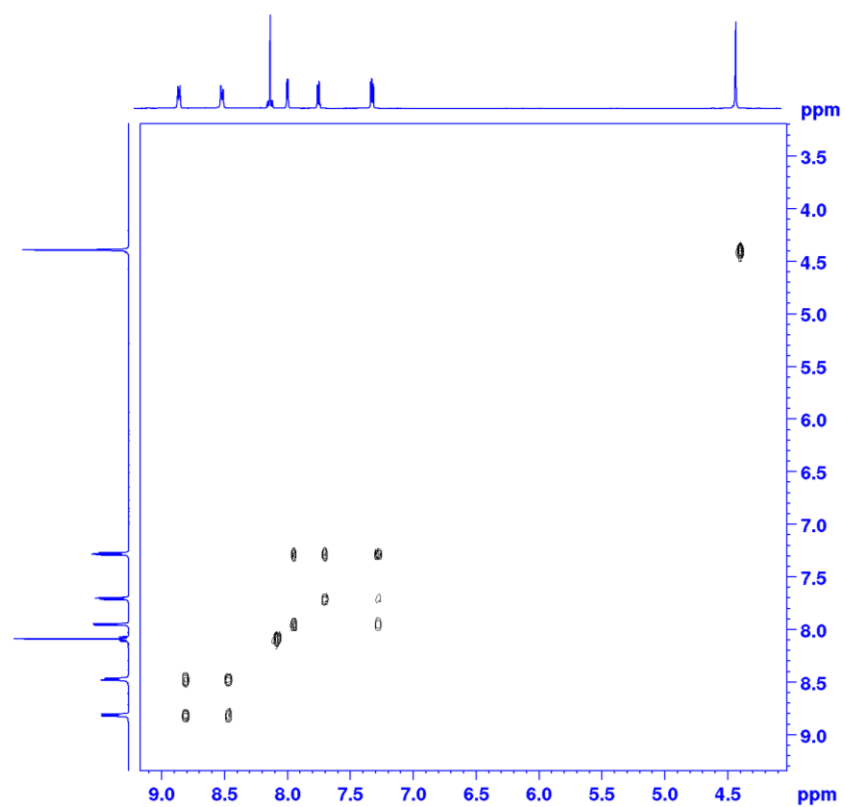
Appendix Five: ^{1}H-^{13}C HSQC-NMR of Hg^{2+}-L
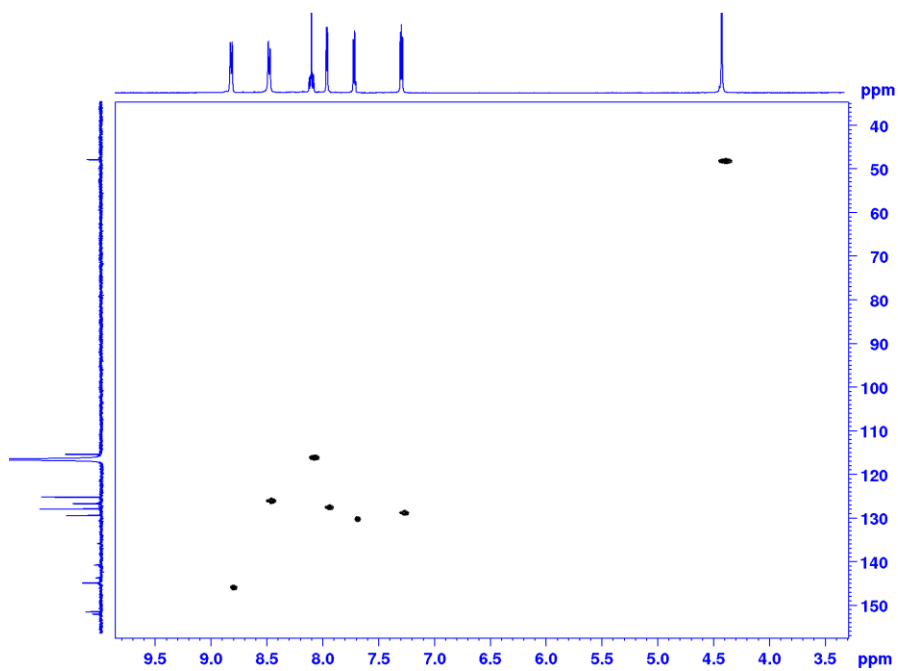

Appendix Six: DEPT135 of Hg^{2+}-L

Appendix Seven: ^{1}H-NMR of Hg^{2+}-QL

Appendix Eight: ^{13}C{H}-NMR of Hg^{2+}-QL

Appendix Nine: ^{1}H-^{1}H COSY of Hg^{2+}-QL

Appendix Ten: ^{1}H-^{13}C HSQC of Hg^{2+}-QL
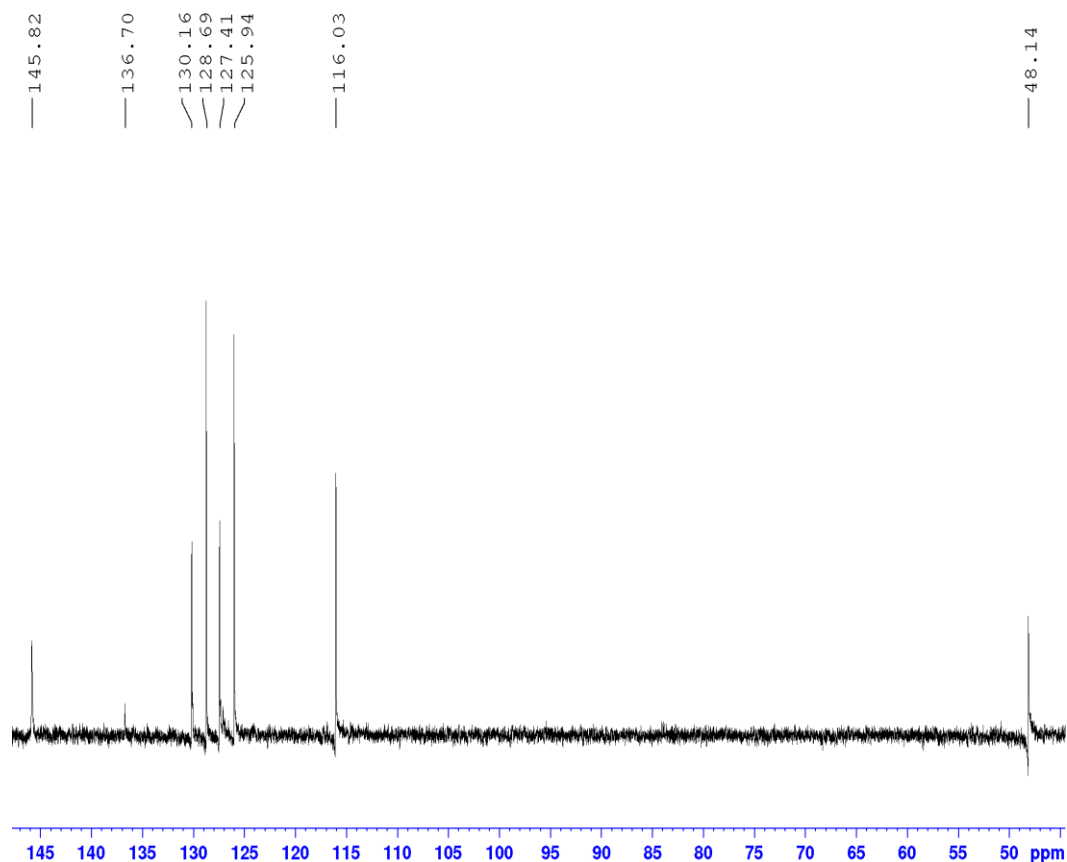
Appendix Eleven: DEPT135 of Hg^{2+}-QL
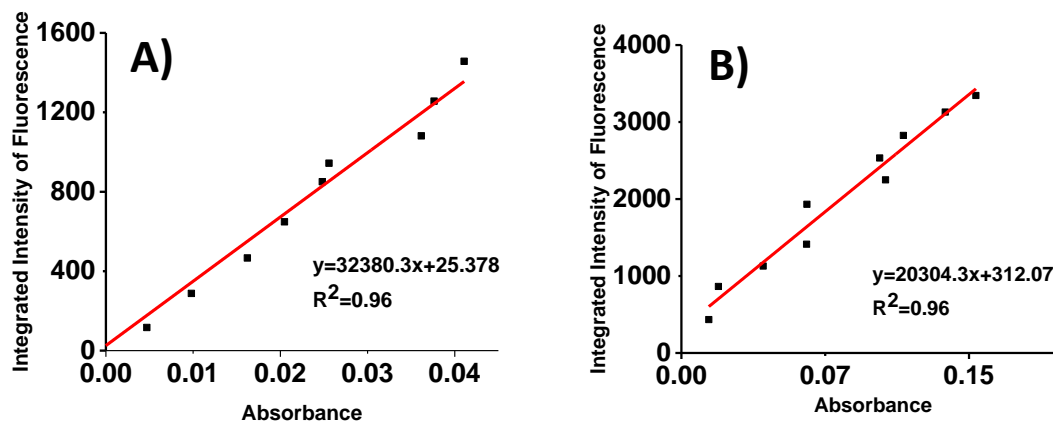
Appendix Twelve: Quantum Yield Calibration Curves for **A)** Hg^{2+}-L complex **B)** Ru(bipy)$_3$ Standard

Appendix Thirteen: Variables for calculation of the standard deviation from quantum yield for Hg^{2+}-L complex

Parameter	Value	Standard Error ($\pm$)
Quantum Yield, ϕ_x, L-Hg(II) Complex	0.57	To be determined

m_x	3.24 x 10^4	2.05 x 10^3
m_{STD}	2.03 x 10^4	1.31 x 10^3
ϕ_{STD}	0.36	0.01
$\sigma_{mx} = standard\ error\ of\ m_x\ * \sqrt{N}$	6.48 x 10^3	-
$\sigma_{mSTD} = standard\ error\ of\ m_{STD}\ * \sqrt{N}$	4.14 x 10^3	-

The standard deviation from quantum yield for Hg^{2+}-L complex was calculated using the equation 1 below:
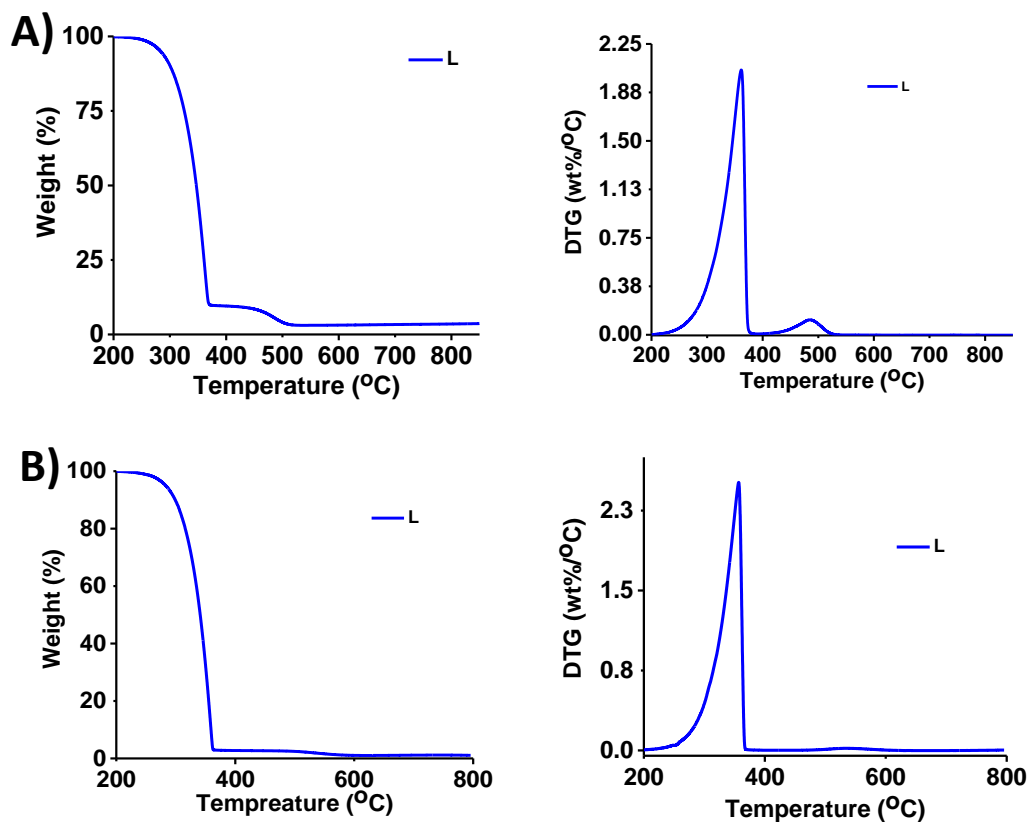
$$\sigma_x = \varphi_x \sqrt{\left(\frac{\sigma_{mx}}{m_x}\right)^2 + \left(\frac{\sigma_{mSTD}}{m_{STD}}\right)^2 + \left(\frac{\sigma_{\varphi STD}}{\varphi_{STD}}\right)^2} \qquad (1)$$

$$\sigma_x = \varphi_x \sqrt{\left(\frac{\sigma_{mx}}{m_x}\right)^2 + \left(\frac{\sigma_{mSTD}}{m_{STD}}\right)^2 + \left(\frac{\sigma_{\varphi STD}}{\varphi_{STD}}\right)^2}$$
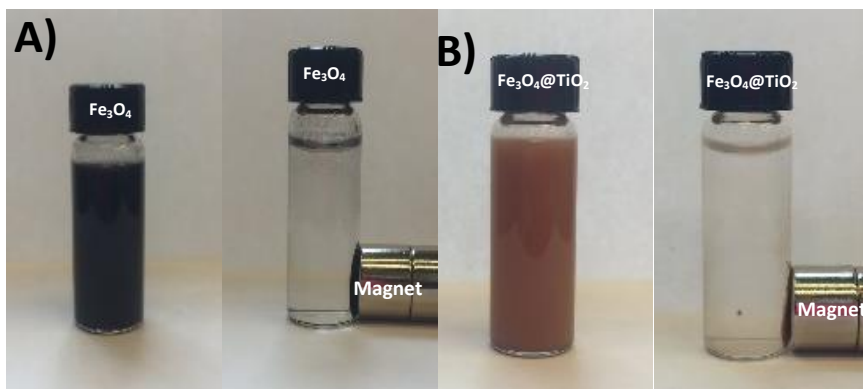
$$= 0.57 \sqrt{\left(\frac{6.48 \times 10^3}{3.24 \times 10^4}\right)^2 + \left(\frac{4.14 \times 10^3}{2.03 \times 10^4}\right)^2 + \left(\frac{0.01}{0.36}\right)^2} = 0.16$$
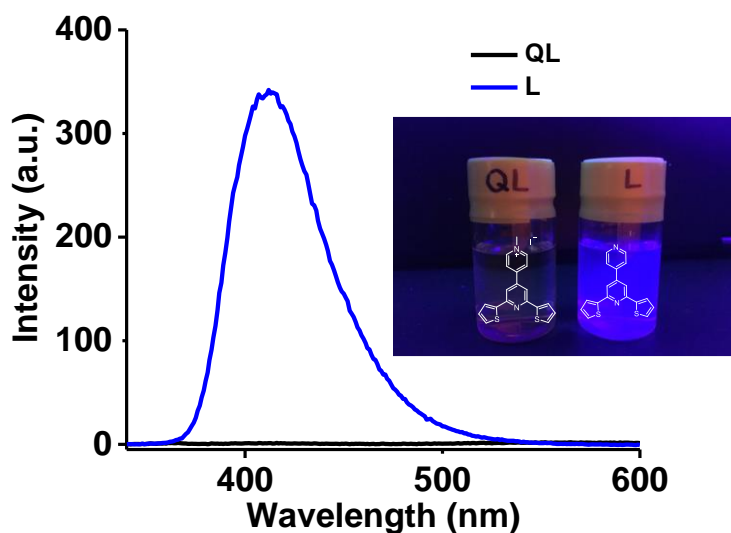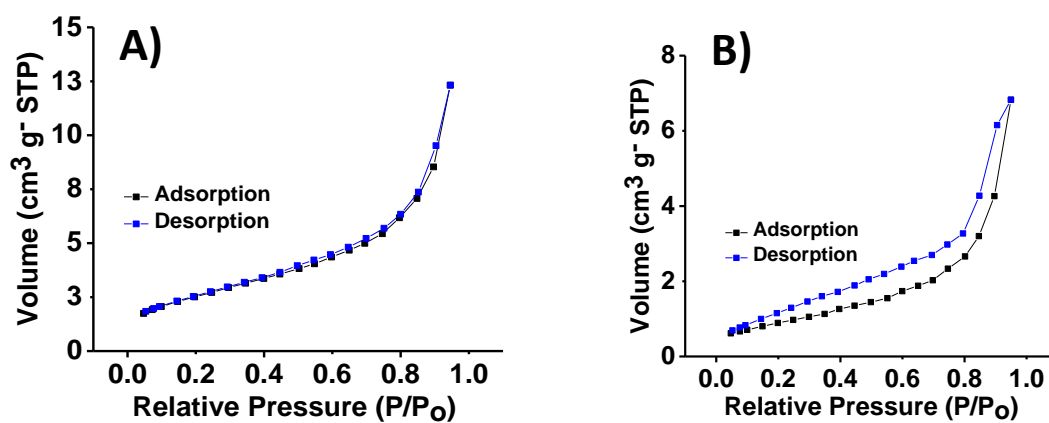

Appendix Fourteen: Fluorescence spectra of Quarternized L (QL) compared to L in ACN with λ_{exc}=330 nm
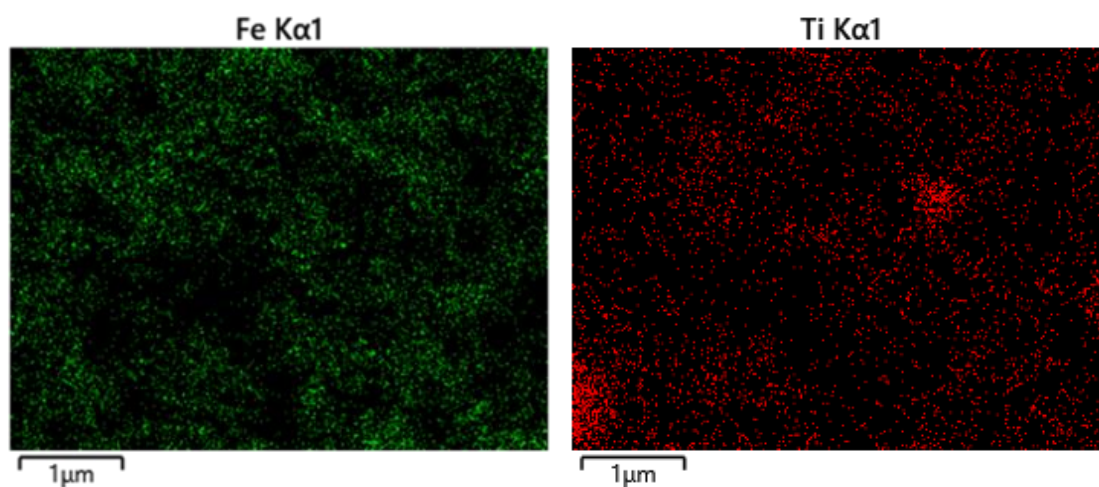
Appendix Fifteen: **A)** TGA analysis of L and DTG analysis L under Air **B)** TGA analysis of L and DTG analysis of L under Argon

Appendix Sixteen: **A)** Photo of Fe_3O_4 before and after magnetic separation in water **B)** Photo of $Fe_3O_4@TiO_2$ before and after magnetic separation in water

Appendix Seventeen: BET analysis of **A)** Fe_3O_4 and **B)** $Fe_3O_4@TiO_2$ with N_2 as the adsorbate

Appendix Eighteen: EDX mapping of $Fe_3O_4@TiO_2$ NP